

The *Blue Jay* Survey: Deep JWST Spectroscopy for a Representative Sample of Galaxies at Cosmic Noon

Sirio Belli¹, Letizia Bugiani^{1,2}, Minjung Park^{3,4,5}, J. Trevor Mendel^{6,7}, Rebecca L. Davies^{7,8}, Amir H. Khoram^{1,2}, Benjamin D. Johnson³, Joel Leja^{9,10,11}, Sandro Tacchella^{4,5}, Vanessa Brown¹², Charlie Conroy³, Razieh Emami³, Yijia Li^{9,10}, Caterina Liboni¹, Gabriel Maheson^{4,5}, Elijah P. Mathews^{9,10,11}, Rohan P. Naidu¹³, Erica J. Nelson¹², Bryan A. Terrazas¹⁴, and Rainer Weinberger¹⁵

¹ Dipartimento di Fisica e Astronomia, Università di Bologna, Bologna, Italy

² INAF, Osservatorio di Astrofisica e Scienza dello Spazio, Bologna, Italy

³ Center for Astrophysics | Harvard & Smithsonian, Cambridge, MA, USA

⁴ Kavli Institute for Cosmology, University of Cambridge, Cambridge, UK

⁵ Cavendish Laboratory, University of Cambridge, Cambridge, UK

⁶ Research School of Astronomy and Astrophysics, Australian National University, Canberra, ACT, Australia

⁷ ARC Centre of Excellence for All Sky Astrophysics in 3 Dimensions (ASTRO 3D)

⁸ Centre for Astrophysics and Supercomputing, Swinburne University of Technology, Hawthorn, Victoria, Australia

⁹ Department of Astronomy and Astrophysics, The Pennsylvania State University, University Park, PA, USA

¹⁰ Institute for Gravitation and the Cosmos, The Pennsylvania State University, University Park, PA, USA

¹¹ Institute for Computational and Data Sciences, The Pennsylvania State University, University Park, PA, USA

¹² Department for Astrophysical and Planetary Science, University of Colorado, Boulder, CO, USA

¹³ MIT Kavli Institute for Astrophysics and Space Research, Cambridge, MA, USA

¹⁴ Department of Physics & Astronomy, Oberlin College, Oberlin, OH, USA

¹⁵ Leibniz Institute for Astrophysics, Potsdam, Germany

October 15, 2025

ABSTRACT

We present the Blue Jay survey, a Cycle-1 JWST program aimed at studying the stellar and gas content of galaxies at Cosmic Noon. The survey consists of deep spectroscopy for 153 targets observed over two pointings in the COSMOS field using the NIRSpec micro-shutter assembly (MSA). We employ the three medium-resolution gratings G140M, G235M, and G395M, with exposure times of 13 hours, 3.2 hours, and 1.6 hours, respectively. We thus obtain full coverage of the 1 - 5 μ m range, corresponding to the entire rest-frame optical wavelength range, with a spectral resolution $R \sim 1000$. Parallel observations provide deep, multi-band NIRCam imaging, which partially overlaps with the spectroscopic observations. The sample is carefully selected to provide a census of galaxies over the redshift range $1.7 < z < 3.5$ above a redshift-dependent minimum stellar mass that ranges from $10^{8.7} M_{\odot}$ to $10^{9.3} M_{\odot}$. The selection ensures that the Blue Jay sample is representative of the entire galaxy population at these redshifts, without strong biases in color, star formation rate, or other properties. The sizes of massive galaxies at these redshifts are comparable to, or larger than the NIRSpec shutters, which requires custom strategies for designing and reducing the observations. Since the standard $A - B$ nod subtraction leads to flux self-subtraction for large galaxies, we construct a master background from empty shutters and subtract it from each of the science spectra. This, in turn, allows for the use of shorter slitlets consisting of only two shutters per galaxy instead of the usual three, with a substantial increase in the multiplexing of the NIRSpec MSA. Another problem introduced by the small shutter size is the mismatch between the galaxy region probed by NIRSpec and that probed by photometric measurements. For this reason, we measure multi-band photometry using archival JWST and Hubble Space Telescope observations in two different ways: *source photometry* is measured in a large elliptical aperture encompassing the entire source, while *box photometry* is measured from the exact area in the sky where the NIRSpec 1D spectrum is extracted. This enables self-consistent fits of spectroscopic and photometric data. The Blue Jay dataset, which we publicly release, represents the ideal sample for studying the stellar populations, neutral gas, and ionized gas in Cosmic Noon galaxies, including star formation histories, quenching, outflows, metallicity, and dust attenuation.

Key words. Galaxies: high-redshift – Galaxies: stellar content – Galaxies: ISM – Surveys – Techniques: spectroscopic – Astronomical instrumentation, methods and techniques

1. Introduction

Cosmic Noon is one of the most interesting and consequential phases in the history of the universe, since about half of the present stellar mass was formed during this relatively short period, corresponding roughly to the redshift range $1 < z < 3$ (Madau & Dickinson 2014). Cosmic Noon is, by definition, the peak of the cosmic star formation history, but it is also the epoch

when the cosmic black hole accretion rate is at its peak (Delvecchio et al. 2014), and when the population of massive galaxies becomes dominated by quiescent systems (Muzzin et al. 2013; Ilbert et al. 2013).

This redshift range, however, is also observationally challenging, because the rest-optical spectral features that contain most of the information about the physical properties of a galaxy are redshifted into the near-infrared, where the CCD sensitivity

quickly declines, and ground-based observations are plagued by atmospheric absorption and emission. For sufficiently high redshift, strong far-UV features such as the Ly α emission line and/or the Lyman break enter the optical window and make it relatively easy to study star-forming galaxies. But at $z \sim 1 - 3$, there are no strong spectral features falling in the observed optical window, and even measuring galaxy redshifts becomes difficult. For this reason, this epoch was dubbed the Redshift Desert (e.g., [Stern & Spinrad 1999](#); [Steidel et al. 2004](#)).

In the last two decades, the development of sensitive near-infrared detectors enabled the characterization of increasingly larger and more diverse samples of galaxies in the $1 < z < 3$ range, thus transforming this epoch from a hostile Redshift Desert to an exciting Cosmic Noon. A considerable amount of time on large ground-based telescopes has been devoted to spectroscopic surveys, which can be broadly divided into two categories according to whether they target the star-forming or the quiescent galaxy population.

The majority of spectroscopic observations at Cosmic Noon focus on star-forming galaxies, which are studied via the emission lines produced by ionized gas. The main challenge is represented by the effect of the Earth's atmosphere, which offers only limited wavelength ranges free from absorption (due to water vapor) and emission (due to OH molecules). As a result, it has been nearly impossible to observe a complete set of strong emission lines *in the same galaxy*. Nonetheless, rest-frame optical emission lines have been detected (and, in many cases, spatially resolved) for samples of hundreds or even thousands of galaxies at $1 < z < 3$ ([Förster Schreiber et al. 2009](#); [Steidel et al. 2014](#); [Kriek et al. 2015](#); [Wisnioski et al. 2015](#); [Curti et al. 2020](#); see [Förster Schreiber & Wuyts 2020](#) for a review).

On the other hand, a subset of spectroscopic studies have focused on quiescent galaxies at $z > 1$, which are gas-poor and lack strong emission lines; their study is thus mostly based on the detection of stellar absorption lines in the galaxy continuum emission. These observations are made particularly challenging by the combination of atmospheric contamination and the requirement of extraordinarily long exposure times, which are needed in order to detect absorption lines against the faint stellar continuum. Additionally, the number density of quiescent galaxies quickly decreases with redshift, limiting the multiplexing capabilities of multi-object spectrographs on large telescopes. As a result, the samples of quiescent galaxies at Cosmic Noon that have been characterized spectroscopically are small, of the order of tens of galaxies (e.g. [Onodera et al. 2012](#); [van de Sande et al. 2013](#); [Bezanson et al. 2013](#); [Belli et al. 2014, 2017](#); [Carnall et al. 2019](#); [Mendel et al. 2020](#); [Kriek et al. 2024](#)).

The advent of JWST enabled spectacular progress in spectroscopic studies of galaxies at $z > 1$, in particular because of the exceptional capabilities of the NIRSpec instrument. The lack of atmospheric absorption and emission means that JWST spectra are more sensitive and can access a wider wavelength range compared to previous ground-based observations. Moreover, while ground-based near-infrared spectrographs typically employ a high spectral resolution ($R \gtrsim 3000$) to isolate the contamination from atmospheric OH emission lines, JWST can employ intermediate ($R \sim 1000$) and even low ($R \sim 100$) spectral resolution, which minimizes detector noise. Finally, the absence of atmospheric seeing means that each high-redshift galaxy creates a much smaller footprint on the detector, enabling a substantially larger multiplexing and higher flexibility in target selection compared to ground-based instruments with the same field of view. Starting with JWST Cycle 1, the NIRSpec Multi-Object Spectroscopy (MOS) mode has been used by several pro-

grams to build samples of galaxies at Cosmic Noon, such as the CECILIA ([Strom et al. 2023](#)), AURORA ([Shapley et al. 2025](#)), and MARTA ([Cataldi et al. 2025](#)) surveys, which targeted mostly emission-line galaxies, and SUSPENSE ([Slob et al. 2024](#)), which instead focused on absorption-line galaxies. Each survey differs in terms of observation depth, wavelength coverage and, crucially, sample selection. Observational programs are typically driven by a specific science goal and therefore tend to target a specific population of galaxies. This ensures the success of the primary goal of the survey, but it also produces a galaxy sample that is typically biased.

In this article we present the Blue Jay survey, a Cycle-1 program (GO 1810, PI: S. Belli) that collected deep NIRSpec spectra over the 1-5 μm wavelength range for a sample of about 150 galaxies at $1.7 < z < 3.5$. Instead of focusing on a particular galaxy population, the Blue Jay survey was designed with the goal of probing a representative sample of galaxies uniformly spanning the target range in redshift and mass, irrespective of other properties such as color or star formation rate. This makes the Blue Jay sample ideal for studying a wide array of aspects related to galaxy evolution, and ensures that the results are sufficiently general to apply to the overall galaxy population, without being driven by a bias in the target selection.

We present the survey design, sample selection, and data reduction in the present work, while the result of spectral fits, both to the continuum and to individual emission lines, are presented in a companion paper by Bugiani et al. (2025, in prep.). Several results have already been obtained using the Blue Jay observations, focusing in particular on the massive end of the galaxy sample. The deep Blue Jay spectroscopy enabled the discovery of widespread neutral outflows ([Davies et al. 2024](#); [Liboni et al. 2025](#)), which are likely responsible for galaxy quenching ([Belli et al. 2024](#)); the detailed study of star formation histories ([Park et al. 2024](#)) and ionized gas ([Bugiani et al. 2025](#)) in quiescent galaxies; and the dust attenuation properties of galaxies at Cosmic Noon ([Maheson et al. 2025](#)).

We describe the sample selection and the JWST observations in Section 2; the NIRSpec data reduction in Section 3; the self-consistent spectroscopic and photometric data set in Section 4. In Section 5 we review the main properties of the Blue Jay sample. Finally, we summarize the characteristics of the survey and briefly describe the main science results in Section 6.

2. Survey Design and Observations

2.1. Guiding Principles

The main goal of the Blue Jay survey is to probe the full set of rest-optical absorption and emission lines for an unbiased, representative sample of more than 100 galaxies at Cosmic Noon. In order to achieve this goal, we make the following choices:

- Given the high signal-to-noise ratio (SNR) on the continuum that is required to detect absorption lines, we adopt the medium-resolution gratings ($R \sim 1000$). This resolution is sufficient to detect significant absorption and emission lines, and at the same time yields substantially higher sensitivity compared to the high-resolution gratings ($R \sim 2700$), because the continuum flux is spread over fewer pixels and is thus affected by lower read-out noise, which is the dominant source of uncertainty. The primary disadvantage is that we are unable to resolve the kinematics below the instrumental resolution of $\sigma_{\text{inst}} \sim 130 \text{ km/s}$. To overcome this limitation, follow-up observations at higher resolution with the G235H

grating have been obtained in Cycle 3 by program GO 5427 (PI: R. Davies).

– We employ all three NIRSpec gratings with medium resolution (G140M, G235M, G395M) to observe the wide wavelength range of 1 to 5 μm , so that all the spectral features of interest are captured by the NIRSpec spectra. This sets a lower limit on the redshift of the sample at $z \sim 1.7$, because below this redshift the [O II] emission line, the bluest among the strong nebular lines, lies outside the wavelength range that can be observed with the G140M/F100LP grating/filter combination.

- The sample selection must be performed with particular care in order to avoid any bias. This requires a complete parent sample that is well characterized at least in terms of redshift and stellar mass. Since Blue Jay was executed in the first half of Cycle 1, the parent sample was necessarily based on pre-JWST data. Deep imaging in the near-infrared was only available up to a wavelength of 1.6 μm , corresponding to the F160W filter on the Hubble Space Telescope (HST). This sets an upper limit on the redshift range, because beyond $z \sim 3.5$ the Balmer break is redshifted past F160W, making the parent catalog highly incomplete.
- The only fields with sufficiently deep multi-band imaging, including near-infrared data from HST, are those observed by the CANDELS survey. Among these, we select the COSMOS field because, being an equatorial field, can be observed from both hemispheres thus maximizing the potential for ground-based follow-up studies.
- To obtain a relatively large sample without sacrificing the exposure time, it is crucial to maximize the multiplexing capabilities of the NIRSpec micro-shutter assembly (MSA). Some programs achieve this by allowing spectral overlap among different sources (e.g. [Cataldi et al. 2025](#); [de Graaff et al. 2025](#)); this strategy can work for sparse emission lines but is not applicable in our case since overlapping continuum traces would be unusable. Instead, we opt for reducing the number of shutters allocated to each source from the standard three to just two. This choice reduces the availability of local background, but this is not an issue since we adopt a master background, as described in detail in Section 3.

In this section we describe how the parent catalog was constructed; explain how it was used to design the NIRSpec pointings; and describe the observational setup.

2.2. Parent Catalog

The sample selection is based on the HST F160W imaging obtained by the CANDELS survey ([Grogin et al. 2011](#); [Koekemoer et al. 2011](#)), adopting the source catalog for the COSMOS field produced by the 3D-HST team (v4.1.5; [Brammer et al. 2012](#); [Skelton et al. 2014](#); [Momcheva et al. 2016](#)). This catalog, which we call the “CANDELS/COSMOS” catalog, includes 33879 sources. In the remainder of this work we adopt the IDs from this catalog to refer to individual sources.

First, we improve the position measurement of the sources in the CANDELS/COSMOS catalog in order to ensure a secure acquisition of the targets observed with NIRSpec. Since the astrometric precision of the CANDELS mosaic in the COSMOS field does not meet the NIRSpec requirements, we make use of the newer mosaic released by the 3D-DASH team ([Mowla et al. 2022](#)), with a pixel scale of 100 milliarcsec. The mosaic extends over a wider field of view (targeted by the 3D-DASH survey), however we focus only on the CANDELS/COSMOS

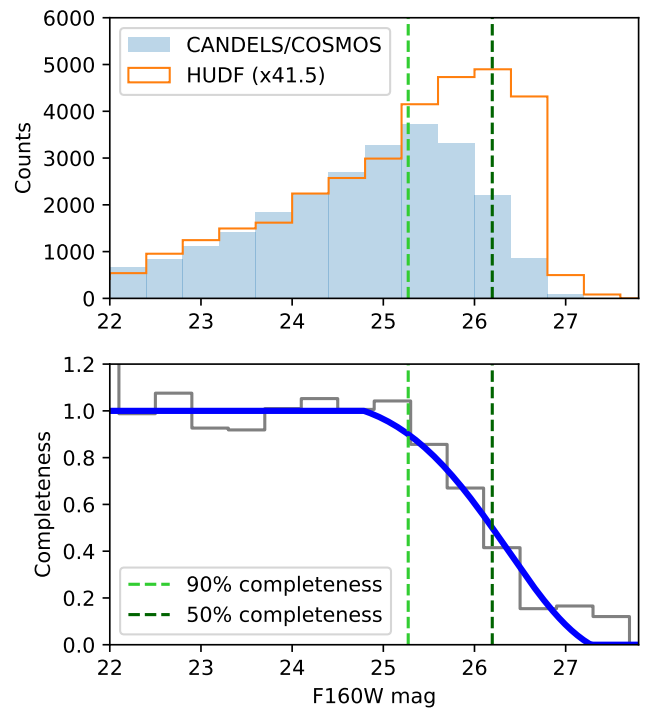


Fig. 1: Assessing the completeness of the CANDELS/COSMOS catalog. Top: source count for the CANDELS/COSMOS and the HUDF catalogs, as a function of the F160W magnitude. The HUDF source counts have been normalized to account for the smaller area. Bottom: we estimate the completeness of the catalog by taking the ratio of the source counts shown in the top panel. The blue line represents a B-spline fit. The vertical dashed lines mark the 90% and 50% completeness limits.

footprint, where the mosaic includes the same data used for the original CANDELS mosaic. We use `forcepho` (B. D. Johnson et al. in prep.) to fit the surface brightness distribution for each of the 33879 sources in the CANDELS catalog. We then identify 134 Gaia stars in the field that have well-measured proper motions in DR3 ([Gaia Collaboration et al. 2023](#)), and are well fit by `forcepho`. After correcting for proper motion, we detect a small shift between the DASH mosaic and the Gaia astrometry ($\Delta\text{RA} = -29$ mas, $\Delta\text{dec} = 7$ mas). We apply this offset to the entire catalog of coordinates measured by `forcepho`, and adopt these as the final coordinates for the parent catalog. Comparing the final coordinates of the stars with those from the Gaia catalog, we find a median absolute deviation of 12 mas on each coordinate.

Second, we estimate the completeness of the F160W detections in the CANDELS/COSMOS catalog by comparing the source count to that from a substantially deeper catalog (as done by, e.g., [Skelton et al. 2014](#); [Tal et al. 2014](#)). For this purpose we adopt the 3D-HST catalog for the GOODS-South field, where we select all sources that lie within the small footprint of the Hubble Ultra Deep Field (HUDF), which was observed with a considerably longer exposure time. The top panel of Figure 1 shows the number of sources flagged as “usable” and with $\text{SNR} > 5$, as a function of F160W magnitude for the CANDELS/COSMOS catalog and the deeper HUDF catalog, after a normalization to account for the smaller HUDF area. The two catalogs are very similar down to about $H \sim 25$, beyond which the CANDELS/COSMOS source count begins to deviate due to incompleteness. In the bottom panel we estimate the complete-

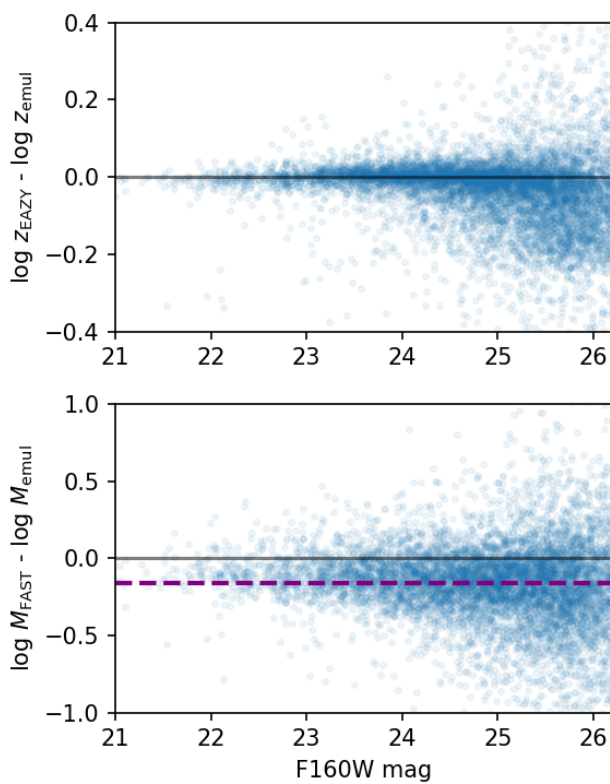


Fig. 2: Discrepancy in photometric redshift (top) and stellar mass (bottom) between the values in the 3D-HST catalog and those from the `Prospector` emulator, as a function of magnitude, for all galaxies in the parent catalog with redshift in the range $1.7 < z < 3.5$. The stellar mass discrepancy is -0.16 dex (median value, shown by the dashed purple line).

ness of CANDELS/COSMOS by taking the ratio of the source counts in the two catalogs (gray histogram), and then fitting a B-spline to obtain a smooth representation (blue curve). This lets us estimate that the CANDELS/COSMOS catalog is 90% complete at $H_{90} = 25.3$ and 50% complete at $H_{50} = 26.2$, in good agreement with the values found by [Skelton et al. \(2014\)](#) using slightly different methods.

Finally, we construct the parent catalog by taking all objects in the CANDELS/COSMOS catalog that fulfill the following requirements:

- Are flagged as “usable” (`use_phot=1`) by [Skelton et al. \(2014\)](#), which means that they are detected in F160W, are not identified as stars or too close to a bright star, are well exposed in F125W and F160W, and have meaningful fits to the photometry;
- Have a SNR in F160W larger than 5;
- Are brighter than $H_{50} = 26.2$, to avoid probing galaxy populations that are mostly undetected in the CANDELS data.

The parent catalog defined in this way consists of 23755 sources.

2.3. Physical Properties of the Parent Sample

The Blue Jay sample selection is based only on stellar mass and redshift, which can be derived from fits to the Spectral Energy Distribution (SED) of each source. The 3D-HST catalog, in addition to the multi-band HST CANDELS data, includes other

ground- and space-based observations for a total of 27 broad bands and 17 medium bands, spanning the optical and near-infrared wavelength range. Using this photometric data set, the 3D-HST team has derived photometric redshifts with the EAZY code ([Brammer et al. 2008](#)) and stellar masses with FAST ([Kriek et al. 2009](#)); see [Skelton et al. \(2014\)](#) for details.

However, the assumptions used by the FAST fitting code, particularly the idealized exponentially declining SFHs, are known to bias the resulting stellar masses ([Leja et al. 2019](#)). This makes the FAST masses inconsistent with those measured using the `Prospector` code ([Leja et al. 2017; Johnson et al. 2021](#)) assuming non-parametric SFHs, as done for the Blue Jay survey (see [Park et al. 2024; Bugiani et al. in prep.](#)). Thus, to ensure self-consistency, we derive new stellar masses and photometric redshifts for the parent sample.

Running `Prospector` on the entire parent sample would require an extremely large amount of computational resources. Instead, we make use of an artificial neural network emulator as described in [Mathews et al. \(2023\)](#). The emulator is trained on a subset of galaxies that are fit with `Prospector` using the FSFS library ([Conroy et al. 2009; Conroy & Gunn 2010](#)). The emulator is then able to produce an approximate posterior distribution for all the parameters in the `Prospector` model, given the observed photometry of a source, in a fraction of the computing time compared to directly running `Prospector`.

Figure 2 shows a comparison of the emulator results with those present in the 3D-HST catalog. The photometric redshifts are approximately consistent, with an increasing scatter for fainter magnitudes. On the other hand, the stellar masses present a systematic offset, with FAST yielding masses that are ~ 0.16 dex (median value) lower than those obtained with the emulator, with substantial scatter even at the bright end. These results are consistent with previous analysis of `Prospector` measurements compared to EAZY redshifts ([Wang et al. 2024](#)) and FAST masses ([Leja et al. 2019](#)). For the remainder of the article we adopt the emulator redshift and masses for the parent sample.

2.4. Spectroscopic Weights

Due to the large number of observable targets and the complex geometric requirements, NIRSpec pointings are determined automatically using an algorithm that maximizes the total weight of the selected targets. Such spectroscopic weights thus represent the relative probability of being selected for observations for each object in the parent catalog. Since our goal is to construct a spectroscopic sample that spans a wide range of properties, we choose to assign larger weights to galaxies that have values of stellar mass M_* and redshift z that are rare. In practice this means setting the weight of each galaxy to be inversely proportional to the smoothed local density of potential targets on the M_* vs. z plane, which is shown in Figure 3. We also divide the weight by the completeness function $f(H)$, shown in the bottom panel of Figure 1, in order to account for similar targets that cannot be selected because they are missing from the parent sample (this correction is small for the majority of targets, and never exceeds 2 since we do not consider galaxies fainter than H_{50}).

Furthermore, we give zero weight to galaxies outside the chosen redshift range $1.7 < z < 3.5$, and with masses below a completeness limit M_{\min} . We calculate this completeness limit following the method of [Pozzetti et al. \(2010\)](#), as explained in detail in Appendix A. The resulting completeness limit as a function of redshift is $\log M_{\min}/M_{\odot} = 8.13 + 0.34z$, and goes from $\log M_{\min}/M_{\odot} \sim 8.7$ at $z = 1.7$ to $\log M_{\min}/M_{\odot} \sim 9.3$ at $z = 3.5$.

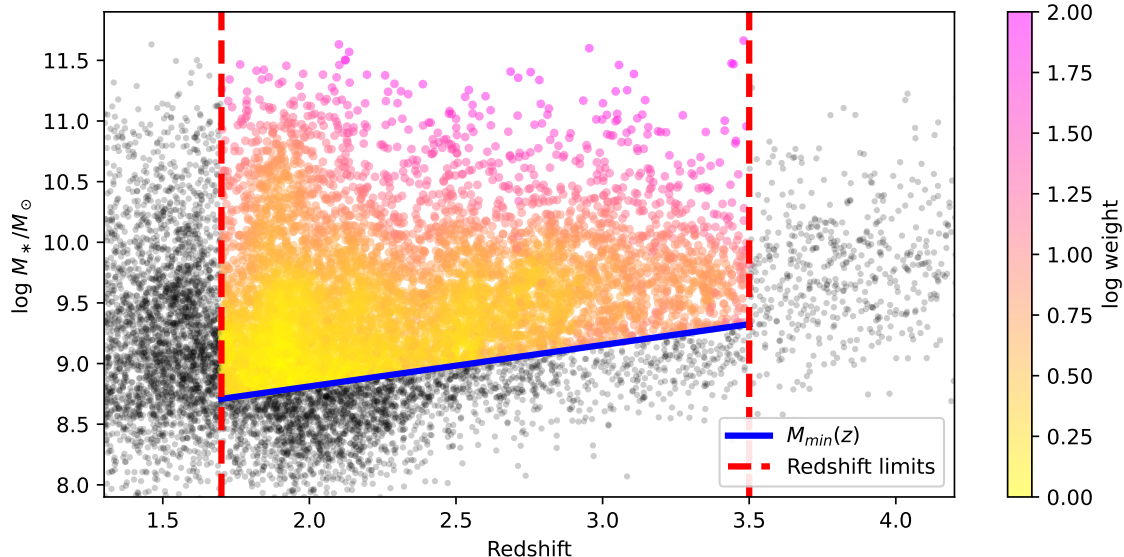


Fig. 3: Distribution of stellar masses and photometric redshifts for the parent sample. The redshift range of the Blue Jay survey, $1.7 < z < 3.5$ is shown in red, while the mass completeness limit is shown in blue. In the region defined by these boundaries, galaxies are color-coded by the spectroscopic weight assigned to them.

We estimate a minor incompleteness for galaxies just above the limit, with $\log M_{\min} < \log M_* < \log M_{\min} + 0.36$, where we may miss about 15% of the total population.

Finally, we scale the weights so that the lowest values are around unity. The resulting weight distribution, shown in Figure 3, spans two orders of magnitude, reaching the largest values in the most massive systems. The sources in the parent sample that have a non-zero weight are 6327.

2.5. Nod Strategy

The MSA shutters are $0.2'' \times 0.46''$, or roughly 1.6×3.8 kpc, a size that is comparable to the typical effective size of galaxies at Cosmic Noon (e.g., van der Wel et al. 2014). This means that the light from a galaxy will often contaminate the adjacent shutters — a problem that affects in particular the most massive galaxies, as illustrated in Figure 4. As a result, adjacent shutters cannot be used to derive a local background. This makes it impossible to adopt the default strategy for NIRSpec observations, which consists of employing 3-shutter slitlets where one shutter is placed on the source and the other two shutters are used to measure the *local* background spectrum. Instead, we decide to perform a *global* background subtraction, using a high-SNR master background spectrum derived from empty shutters, as explained in detail in Section 3.3.

Since we do not make use of a local background, we do not necessarily need to employ the standard 3-shutter slitlet. We adopt, instead, a 2-shutter slitlet, which has the crucial advantage of increasing the multiplexing capabilities of the MSA, since we can allocate 50% more galaxies using the same number of shutters. Moreover, shorter slitlets make the MSA design less prone to disruption by failed shutters (stuck open or stuck closed), leading to more efficient slitlet allocation.

We adopt a 2-point nodding pattern, where the source is placed first on the upper shutter (“nod A”) and then in the lower shutter (“nod B”), as shown in Figure 4. However, when reducing the data (as described in Section 3) we do not perform the usual $A - B$ subtraction, which in our case would lead to self-subtraction of the galaxy flux. Instead we treat the two nod posi-

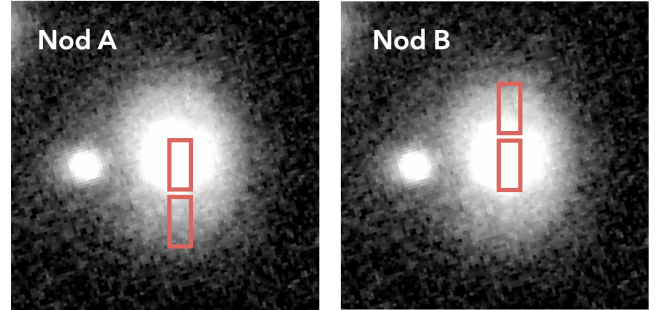


Fig. 4: Footprints of the NIRSpec shutters for galaxy 10592 ($z = 1.8$, $\log M_*/M_\odot = 11.2$), illustrating the 2-point nodding adopted by Blue Jay. Given the large size of the galaxy, it is not possible to derive a local background from shutters adjacent to the primary shutter – instead, a master background must be used. The galaxy image is from NIRCam F200W.

tions as dithers, i.e., we *sum* the flux obtained at the A and the B position. The main goal of dithering is to mitigate the impact of detector defects and flat fielding imperfections.

2.6. Configuration of NIRSpec MSA

We design the NIRSpec pointings using the MSA Planning Tool available on the APT software (version 2022.5.3). We make use of the spectroscopic weights described in Section 2.4 and adopt a 2-shutter slitlet for each source. We do not allow the spectral traces to overlap on the detector, since this would make it impossible to study the continuum emission. However, we do allow spectral overlap due to stuck open shutters, which being empty will cast the background spectrum, potentially contaminating a portion of a science slitlet.

We employ an “unconstrained” source centering criterion, meaning that the source will be allocated to a shutter even if the position in the parent catalog is exactly behind the shutter bar. This increases the efficiency of the MSA configuration, at the

Table 1: Summary of NIRSpec MSA configurations

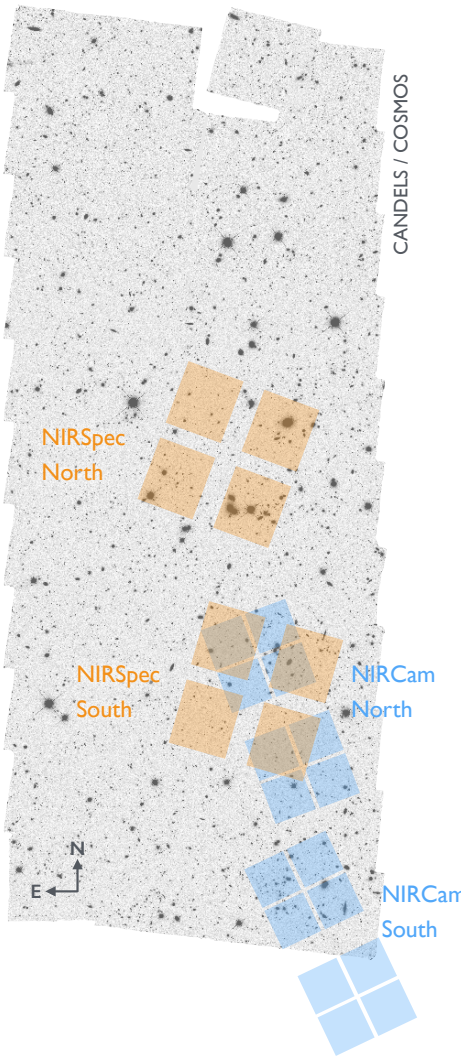


Fig. 5: Blue Jay NIRSpec pointings (in orange; each pointing consists of four MSA quadrants) and parallel NIRCam fields (in blue; each field consists of two separate arrays of 2×2 detectors). The NIRCam North field was observed in parallel to the NIRSpec North pointing. The background image is the HST F160W mosaic of the CANDELS/COSMOS field.

cost of potentially large slit losses. However, since our targets are typically much larger than the $0.07''$ shutter bar width, the slit losses do not depend strongly on the exact position of the source center.

With the chosen settings we are able to observe about 75 targets with a single MSA configuration; to reach the desired sample size of more than 100 galaxies we thus need two NIRSpec pointings. We position the first pointing, dubbed South pointing, near an area densely populated by galaxies with high spectroscopic weights, corresponding to a known overdensity at $z \sim 2.1$ (Spitler et al. 2012). Using the MSA Planning Tool, we search for the optimal position (i.e. the one that maximizes the sum of the spectroscopic weights) using a large grid. We then use this position to start a new search with a finer grid, in an iterative fashion, until we reach a grid step size of 5 mas, which is smaller than the astrometric uncertainty. Once we have established the position of the South pointing, we repeat the procedure for the

	North Pointing	South Pointing
Science		
Slitlets	74 ^a	78 ^b
Shutters	180	191
Background		
Slitlets	38	38
Shutters	63	50

Notes. Slitlet and shutter counts include stuck open shutters.

^a One slitlet composed of a single stuck open shutter (ID 22990).

^b One slitlet contains two galaxies (IDs 11420 and 11451).

North pointing, which we place in such a way so that its parallel NIRCam imaging overlaps the South pointing, as illustrated in Figure 5. This ensures that a fraction of the sample will be observed by both NIRCam and NIRSpec. Moreover, the North pointing is sufficiently far from the $z \sim 2.1$ overdensity to ensure that our sample probes a range of environments at each redshift.

After both pointings have been defined, we analyze the resulting target sample by performing detailed SED fitting with `Prospector`. This is much more computationally demanding compared to the emulator fits described in Section 2.3, but yields more robust results. We find that for a few galaxies the photometric redshift measured by `Prospector` is substantially different than the value predicted by the emulator. In some cases the new redshift is still within the survey limits, but for eight galaxies the new redshift is outside the $1.7 < z < 3.5$ range. We remove these targets from the parent sample and run the MSA Planning Tool once more, using a very small grid to ensure that the majority of the targets are unchanged.

The resulting MSA configurations have a non-negligible fraction of detector area that is not illuminated, and we make manual changes to the MSA plan to take advantage of all the available space on the detector. In some cases we find sources that are nominally outside an available shutter, but close enough to ensure that part of the light emitted by the source will fall in the shutter nonetheless; we manually create slitlets for these targets. We also manually add four high-redshift ($z \sim 6$) targets, taken from a list of candidates identified with a dropout technique. Finally, we systematically open additional empty shutters to be used for the master background, until each row of the detector is illuminated, making sure to avoid any spectral overlap. We achieve this in two ways: first, we manually extend the galaxy slitlets by opening adjacent shutters, if they are available. We are able to do this for about one third of the slitlets, reaching a length of 3, 4, or 5 shutters. Second, in the regions of the MSA that are still available we create new slits on empty parts of the sky, trying to uniformly sample the MSA quadrants.

Table 1 summarizes the number of shutters and slitlets in each of the two pointings. The total number of science slitlets is 152; since in one case two galaxies (both parts of the parent sample) fall in the same slitlet, the total number of galaxies observed with NIRSpec is 153. Due to the manual optimization of the MSA configurations, each science slitlet consists on average of 2.4 shutters. Additionally, there are 76 empty background slitlets, mostly consisting of one or two shutters, including those that are stuck open.

Table 2: Summary of the Primary NIRSpec Observations

Grating/Filter	Integrations per exposure	t_{exposure}	Dithering pattern	N_{exposure}	t_{total}
G140M/F100LP	4	97.2 min	AA'BB'AA'BB'	8	778 min
G235M/F170LP	2	48.6 min	AA'BB'	4	194 min
G395M/F290LP	1	24.3 min	AA'BB'	4	97 min

Notes. Each integration consists of 20 groups in NRSIRS2 mode, corresponding to an integration time of 24.3 min. The dithering positions along the y (cross-dispersion) direction are: $A = +0'.529$, $A' = +0'.539$, $B = 0'.000$, $B' = +0'.010$.

Table 3: Summary of the Parallel NIRCam Observations

Filter	Total integrations	t_{total}
F090W	4	92 min
F115W	8	184 min
F150W	16	368 min
F200W	16	368 min
F277W	12	276 min
F356W	16	368 min
F444W	16	368 min

Notes. Each integration consists of 7 groups in DEEP8 mode, corresponding to an integration time of 22.9 min.

2.7. Primary NIRSpec Observations

We observe the two NIRSpec pointings adopting a 2-point AB nodding pattern, as explained in Section 2.5. We also perform parallel imaging observations with NIRCam, which benefits from sub-pixel dithering in order to improve the spatial resolution. This so-called “compromise dither” adds a second set of positions, $A'B'$, which are slightly offset from the AB positions by $0.01''$ along the cross-dispersion direction. Thus, each NIRSpec observation must include at least four exposures, corresponding to the sequence $AA'BB'$.

We adopt the NRSIRS2 readout pattern with 20 groups per integration, corresponding to the maximum recommended integration time of about 1500 seconds. This is the optimal integration time, because it lowers the read-out noise as much as possible without being negatively impacted by cosmic rays. Using four exposures (because of the $AA'BB'$ pattern adopted) with just one integration each yields an optimal exposure time of about 97 minutes. To maximize the SNR and minimize the overheads, we set the exposure time for each grating to be a multiple of this value, by increasing the number of integrations and/or the number of exposures.

For each of the three gratings we determine the exposure time by requiring a SNR of 10 per \AA for the most massive galaxies in the sample, to ensure that even fainter absorption lines can be robustly measured. Using the JWST exposure time calculator we find that this goal can be achieved in about 13 hours for G140M/F100LP; 3.2 hours for G235M/F170LP; and 1.6 hours for G395M/F290LP, as shown in Table 2. The exposure times are progressively shorter at longer wavelengths due to the combination of brighter continuum (for massive, typically red galaxies) and higher NIRSpec efficiency.

The North and South pointings were observed, respectively, in November and December 2022, under JWST Cycle-1 program GO 1810. The NIRSpec observations are available in the Mikulski Archive for Space Telescopes (MAST) at the Space Telescope Science Institute, and can be accessed via [http://doi.org/10.17909/t11e-xh37](https://doi.org/10.17909/t11e-xh37).

2.8. Parallel NIRCam Imaging

We obtain multi-band NIRCam imaging in parallel to the NIRSpec observations. The CANDELS/COSMOS field is also observed with NIRCam by the PRIMER and COSMOS-Web programs, but the unusual depth of the Blue Jay observations offers the possibility of obtaining exquisite NIRCam imaging. The parallel imaging observations include 41 out of 153 (27%) Blue Jay spectroscopic targets, because the NIRCam fields partially overlap with the NIRSpec pointings by design, as explained in Section 2.6.

Table 3 lists the seven broad-band filters employed in the observations and the corresponding exposure times, which are partially constrained by the primary NIRSpec observations and by the NIRCam design, which allows simultaneous observations of the same field in a short-wavelength band and in a long-wavelength band. In four of the bands we reach an exposure time of about 6 hours each. For details about the NIRCam data, see Conroy et al. (2024). The NIRCam parallel observations are publicly available on MAST: <https://doi.org/10.17909/vzzy-4w25>. Additional medium-band imaging in the F182M and F410M filters obtained by the follow-up program GO 5427 will soon become available.

The position of the South NIRCam field is completely determined by the combination of the primary NIRSpec field location and the position angle assigned to our program. As shown in Figure 5, the South NIRCam field falls partly outside the southwest corner of the CANDELS/COSMOS footprint. A nearby low-mass galaxy, Ark 227, happens to lie in that position: this coincidence enables a uniquely deep study of the outer stellar halo of a local galaxy, carried out by Conroy et al. (2024). In the two NIRCam fields we identify 6044 individual stars belonging to Ark 227, spanning the entire virial radius of the galaxy, up to 100 kpc from the galaxy center. The surface density distribution of the stars reveals the presence of “accretion shelves”, likely due to past minor merger events.

3. Data Reduction

We download the raw NIRSpec observations from MAST and reduce them with the JWST Calibration Pipeline (Bushouse et al. 2024) version 1.17.1, adopting version 1321 of the Calibration Reference Data System. In this section we describe the data reduction, with an emphasis on those steps in which our analysis deviates from the default Calibration Pipeline workflow.

3.1. Slit Definition

The Calibration Pipeline relies on the description of each MSA configuration stored in the corresponding MSA metafile. Before running the pipeline, we apply a number of changes to the default MSA metafiles downloaded from MAST:

- Stuck open shutters are usually not included in the list of slitlets to be reduced. However, we manually added these shutters because they can be used for deriving the master background; moreover, in one case a science target (ID 22990) falls in a stuck open shutter.
- In a few cases we manually opened a shutter when designing the MSA plan because a portion of a galaxy falls in it, despite the catalog position of the target being nominally outside the shutter area (as described in Section 2.6). We mark these shutters as containing a science target, and the relative coordinates were set to be formally inside the shutter footprint, but as close as possible to the catalog coordinates.
- A small number of shutters did not open during the observations, as can be seen from the lack of background flux; these shutters were marked closed in the MSA metafile.
- To each shutter not containing a science target we assign a virtual source, with a unique ID, placed at the center of the shutter in the A nod position. This is purely for bookkeeping purposes and to facilitate the identification of stuck open shutters among the background slits.

3.2. Production of 2D Spectra

The uncalibrated data downloaded from MAST consist of successive, non-destructive reads of the charge in each pixel, and are stored in separate files for the NRS1 and NRS2 detectors. The first stage of the Calibration Pipeline performs detector-level corrections (linearity, dark current, bad pixel masking, etc.); identifies and masks those reads presenting an abrupt jump due to cosmic ray hits; and finally converts the reads to a single measurement of the count rate in each pixel. This yields the *rate* files which contain the traces from all the open MSA shutters. We run the first stage adopting the default parameters of the Calibration Pipeline and turning on the mitigation of large cosmic-ray events (so-called “snowballs”), which are known to affect near-infrared detectors.

One of the limitations of the pipeline is the inability to effectively mask all the bad pixels in the frame. We thus create a bad pixel mask for each detector and each pointing in the following way: we median-stack an equal number of frames obtained with the G140M, G235M, and G395M gratings. Because each grating targets a different wavelength range, when stacking together the data we are removing any sharp spectral features such as emission or absorption lines; however, the continuum traces are visible in the stack. We then identify pixels that are outliers compared to their neighbors along the dispersion direction. This method is similar to the `selfcal` algorithm that is an optional part of the JWST pipeline, but we apply it to the entire frame instead of the individual spectra. We find a number of bad pixels that is of the order of 1% of the total.

Next, we measure the bias in each detector, which we define as the median flux value of all the pixels that are not illuminated. We measure a small but non-zero bias, which varies from exposure to exposure. We subtract the bias from each frame, and find that this improves the consistency of the master background measured from different frames, as discussed below.

After masking the bad pixels and correcting for the bias, we run the second stage of the JWST pipeline, which includes the bulk of the data reduction processes, such as wavelength and flux calibration, resampling, and extraction of the 2D trace for each target. This yields unrectified, but calibrated, 2D spectra (`cal` files), an example of which is shown in the top panel of Figure 6, and rectified 2D spectra (`s2d` files).

We run this stage twice: first, we adopt the standard $A - B$ subtraction, which has the advantage of removing background emission and contamination from stuck open shutters, but suffers from self-subtraction due to the large size of our targets; we use this only as a comparison data set. We then run the pipeline without $A - B$ subtraction and turning off any other type of background subtraction. We use this data set to derive a master background, which we will then use in the final steps of the data reduction.

3.3. Master Background

By design, the Blue Jay survey adopts a master background subtraction strategy to avoid the self-subtraction caused by the standard $A - B$ strategy applied to large target. However, we note that the master background subtraction method is also optimal from the point of view of the SNR, because the master background spectrum can be determined with high accuracy by using a large number of slitlets, while in the $A - B$ subtraction the sky spectrum is determined using a small number of spatial pixels, and so its contribution to the final uncertainty can be non-negligible. For this reason the master background subtraction remains a valid choice even when the slitlets are longer, and is adopted by several surveys such as CECILIA (see discussion in Rogers et al. 2025) and RUBIES (de Graaff et al. 2025).

We construct a master background spectrum for each combination of exposure, grating, detector, and pointing (i.e., for each `cal` file produced by the pipeline). When designing the MSA configuration, we purposefully added empty slitlets for measuring the background spectrum. Additionally, the science slitlets often include a spatial region that is free from emission from the source, either because the source is compact, or because the slit was manually extended with additional shutters in the planning phase, as explained in Section 2.6. Thus, the first step is to identify all the “sky” pixels that are not contaminated by source emission, using the entire set of available 2D spectra.

The selection of sky pixels is illustrated in Figure 6 for an example slitlet composed of two shutters: the upper shutter contains a source while the lower shutter is empty. We start with the unrectified 2D spectrum (top panel), to avoid unnecessary resampling of the data; we then construct the spatial profile along the slit (bottom left panel), smooth it, and automatically identify the presence of sources by using a peak finder algorithm. Next, we exclude pixels that fall in the area of the detector that is not fully illuminated due to the shadow of the MSA bars. In principle, the pipeline applies a `barshadow` correction to the flux in each pixel to account for this effect, but the correction is imperfect and leaves residuals that are visible in the 2D spectrum. We thus exclude pixels with a `barshadow` correction larger than 20%. The remaining pixels are selected as “sky” pixels, and are shown in blue in the bottom panels of Figure 6. Typically these are less than half of the pixels in a slit; their histogram is a normal distribution around a small, positive value. Slitlets containing large sources do not contribute any sky pixel.

Once we have selected the sky pixels in all the available slitlets from a given `cal` file, we combine them to obtain a master background. We first exclude slits where the median sky flux is an outlier compared to the other slits; these are cases where the peak finder algorithm fails due to large and/or multiple sources in the slit. We also exclude pixels that have a large uncertainty, as calculated by the pipeline. The final selection of all sky pixels for a single detector includes a number of pixels of the order of 10^5 ; an example is shown in Figure 7. After removing outlier pixels with a running sigma-clipping, we obtain the master

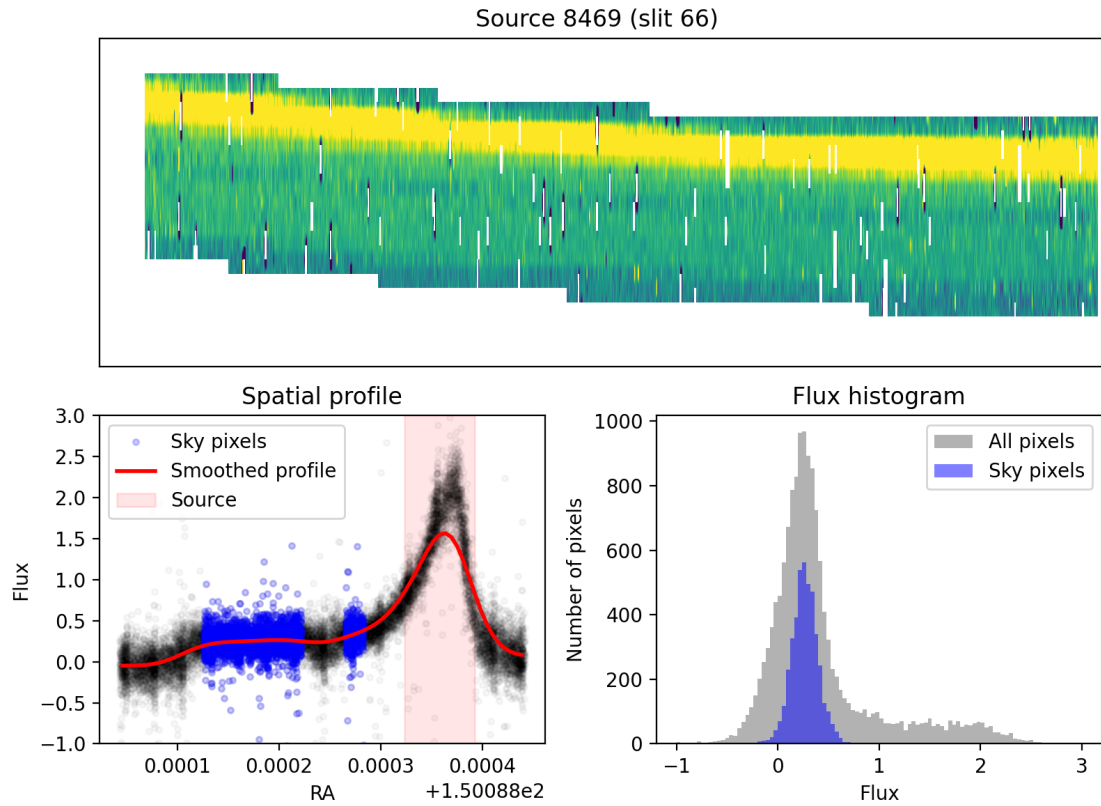


Fig. 6: *Top*: Example of calibrated, unrectified 2D spectrum (ca1 file) produced by the second stage of the pipeline. This is a 2-shutter slit, with a compact galaxy in the top shutter. The shadow of the MSA bar between the two shutters is clearly visible, despite the application of a correction by the pipeline. White vertical stripes are bad pixels (the aspect ratio of the figure is compressed along the horizontal direction in order to visualize the full spectrum). *Bottom*: Selection of the sky pixels from the 2D spectrum. The spatial profile (left panel) is used to identify source emission. Selected sky pixels, shown in blue, are those that are not affected by source emission and bar shadows. They represent less than half of the total pixels, and their fluxes typically have a normal distribution around a small, positive value (right panel).

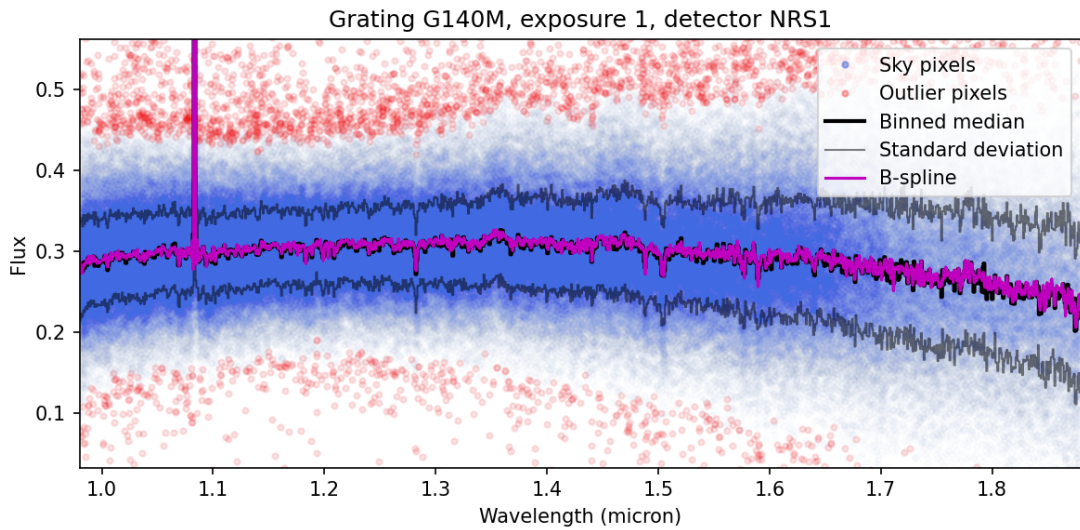


Fig. 7: Example of master background construction for the G140M grating. The figure shows the flux as a function of wavelength for more than 200,000 individual “sky” pixels that were selected from different slits for a given detector and exposure. After removing the outliers (red points), the master background is constructed by fitting a B-spline model (pink line) to the pixel fluxes. The running median (thick black line) and standard deviation (thin black lines) are shown for comparison. The strong emission line visible in the master background is He I at $1.083 \mu\text{m}$.

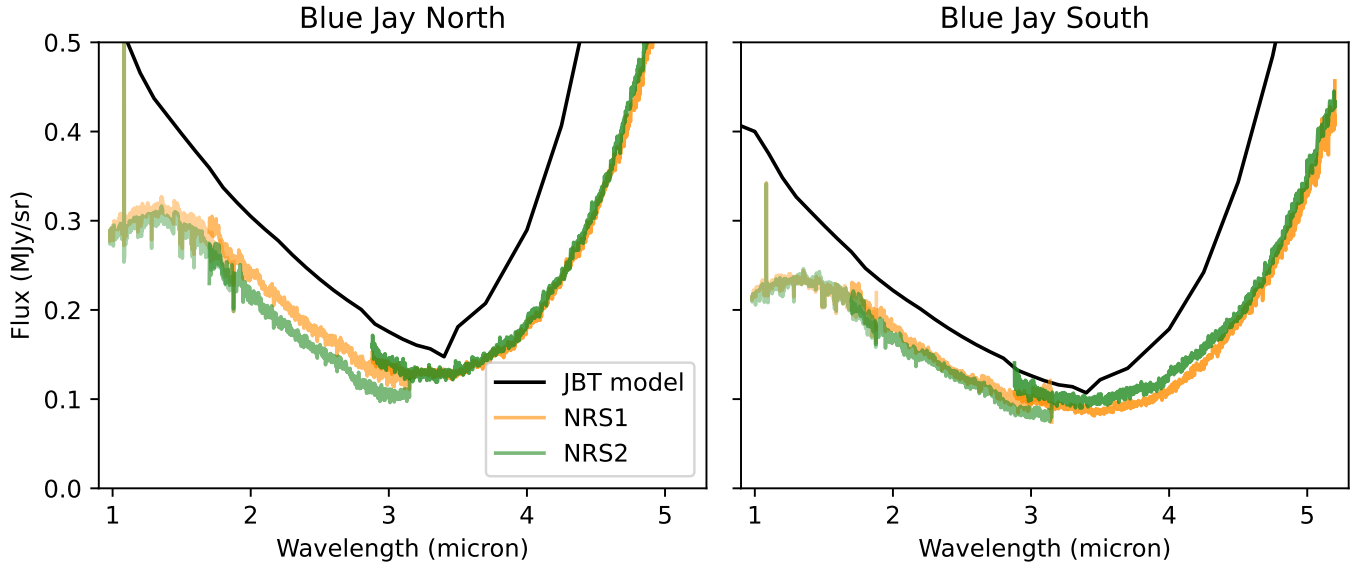


Fig. 8: Master background for the Blue Jay North (left panel) and South (right panel) pointings. The NRS1 and NRS2 master backgrounds are shown separately with different colors; for each detector, the three gratings are plotted with different levels of transparency. The black line is the JBT model generated for the coordinates and observation date of the two pointings.

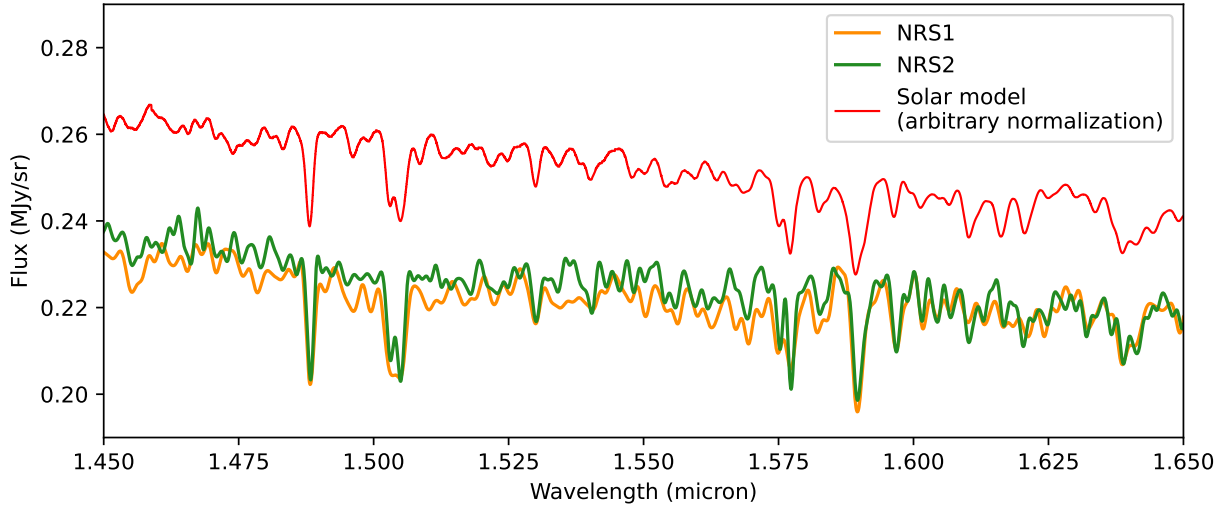


Fig. 9: Zoom-in on a small spectral region of the G140M grating, showing the master background in the South pointing for the NRS1 and NRS2 detectors. For comparison, we show the [Kurucz \(1993\)](#) solar model with a $R \sim 1000$ resolution, after having applied a continuum normalization derived from the JBT, and an arbitrary offset.

background spectrum by fitting a B-spline to the sky pixel flux as a function of wavelength. For comparison, we also bin the sky pixels in wavelength and calculate the running median, finding a consistent result. We estimate the uncertainty by taking the standard deviation of the pixel flux values in each wavelength bin. We then compare this to the median of the pixel flux uncertainties provided by the pipeline. We find that the standard deviation is a factor 1.5-2 larger than the formal uncertainty, indicating that the pipeline underestimates the spectral error, as commonly reported (e.g., [Maseda et al. 2023](#)). We do not correct the spectral uncertainties at this point, because this correction is done by the so-called “jitter” parameter in the **Prospector** fitting, as discussed in [Park et al. \(2024\)](#) and [Bugiani et al. \(2025, in prep.\)](#).

We find that the master background spectrum does not vary systematically from one exposure to another, or from one region of the detector to another. We thus combine all the background spectra into a single master background for each grating. The master background spectra for the two Blue Jay pointings are shown in Figure 8, separately for the NRS1 and NRS2 detectors. For each pointing and grating, the two detectors have slightly different background spectra, by up to 15%; this could be due to small variations of throughput, bias, or other systematics. For this reason, we apply the master background subtraction separately for the two detectors instead of combining them together. We also note a discrepancy in the background at 3 μ m measured from the G235M and G395M filters, present in both the North

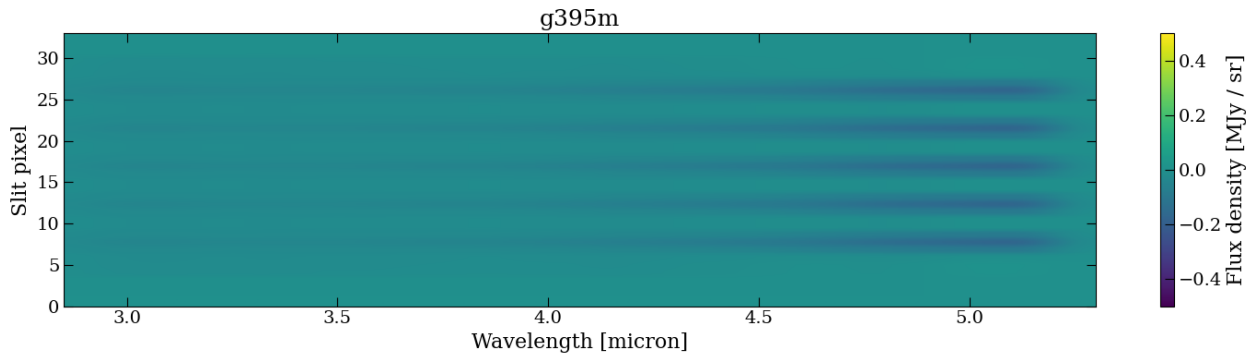


Fig. 10: Stack of all the pixels in empty shutters for the G395M grating, where the pixels have been binned according to their distance from the bar position. The residual background pattern is produced by insufficient bar-shadow attenuation of the master background spectrum. We correct for this effect by subtracting this stack from each 2D spectrum.

and South pointings, which is likely due to imperfect flux calibration.

The master background spectra for the North and South pointings are clearly different in normalization and shape. The intensity of the 1.083 μm He I line, which is the only strong emission line in the sky spectrum, is also different in the two pointings. This is due to physical variations in the background, since the pointings were observed at different times of the year. We use the JWST Backgrounds Tool¹ (JBT) to estimate the expected background level given the coordinates and time of the year of the Blue Jay observations. While the overall shape of the JBT prediction is in broad agreement with the observed background, its normalization is about 20% too high, and the discrepancy increases rapidly at the short wavelength end, as shown in Figure 8. However, these are known issues with the JBT model (Rigby et al. 2023). The observed sky spectrum also contains several absorption lines, which are not modeled by the JBT. These are due to the zodiacal light, which is scattered sunlight and therefore has the same absorption lines that are found in the solar spectrum. To verify this, in Figure 9 we compare a small section of the G140M background spectrum with a solar model (Kurucz 1993). The observed small-scale features clearly match the absorption lines in the solar spectrum. We thus conclude that our procedure is able to recover a robust measurement of the background spectrum.

3.4. Bar Shadow Correction

We run the second stage of the JWST pipeline for the third and last time, turning on the master background subtraction and providing the master background spectrum obtained with the method described above. Finally, we run the third stage of the pipeline which combines different exposures and gratings, and thus obtain fully calibrated, rectified, and background-subtracted 2D spectra. However we noticed that, in the empty slits, pixels affected by the bar shadow have fluxes centered on negative values, instead of zero. This effect is caused by the imperfect bar shadow correction, which the pipeline applies to the master background before subtracting it from the data. Since the pipeline does not sufficiently suppress the background spectrum in the pixels affected by the bar shadow, these pixels end up being oversubtracted. To correct for this issue, we construct a 2D stack using all the empty shutters, and binning each pixel row ac-

cording to their distance from the bar position. The result shows a clear pattern where the pixels that are fully illuminated have fluxes around zero, while those that are closer to the shutter bar have increasingly negative fluxes, particularly towards the red end of the NIRSpec range, where the background flux increases and the point spread function becomes larger (see Figure 10). We subtract this 2D background pattern from each science spectrum. This method substantially mitigates the imprint of the bar shadow on the 2D rectified spectra, however many slitlets still feature flux residuals, either positive or negative, coinciding with the shutter bar position. This appears to be due to a variation in the shape and strength of the bar shadow with position on the MSA, which is not captured by our 2D stack.

The imperfect bar shadow correction remains one of the limiting factors for the accuracy of the Blue Jay spectra. In order to improve on this, a more complex model of the bar shadow correction that is allowed to vary for each slitlet would be required (see, e.g. de Graaff et al. 2025; Rogers et al. 2025).

4. Spectro-Photometric Data Set

Figure 11 shows a select sample of Blue Jay targets as a function of their redshift and mass. The cutouts are made with JWST/NIRCam data (described below); the footprint of the microshutters that make up the MSA slitlet is also displayed. Most slitlets consist of two shutters, which however probe three positions when adding the A and B nods together. In many cases the microshutters are small compared to the target, particularly for galaxies at intermediate and high masses. Moreover, the NIRSpec slitlet is often not centered on the galaxy, either because of geometrical constraints of the MSA (which consists of a fixed grid), or because the source center measured from the HST imaging, which was used for designing the observations, is biased towards blue, star-forming regions. It is thus clear that, at these redshifts, NIRSpec MSA observations of massive galaxies are able to probe only a region, and not necessarily the central one, within the targeted galaxy. This may introduce a bias when analyzing spectroscopy together with broadband photometry, which is typically measured over the entire extent of the galaxy. We solve this problem by developing two different sets of photometric measurements: the *source photometry* is measured in an elliptical aperture encompassing the entire galaxy; while the *box photometry* is measured in the small “box” aperture which is used to extract the NIRSpec data, as explained in this section.

¹ <https://jwst-docs.stsci.edu/jwst-other-tools/jwst-backgrounds-tool>

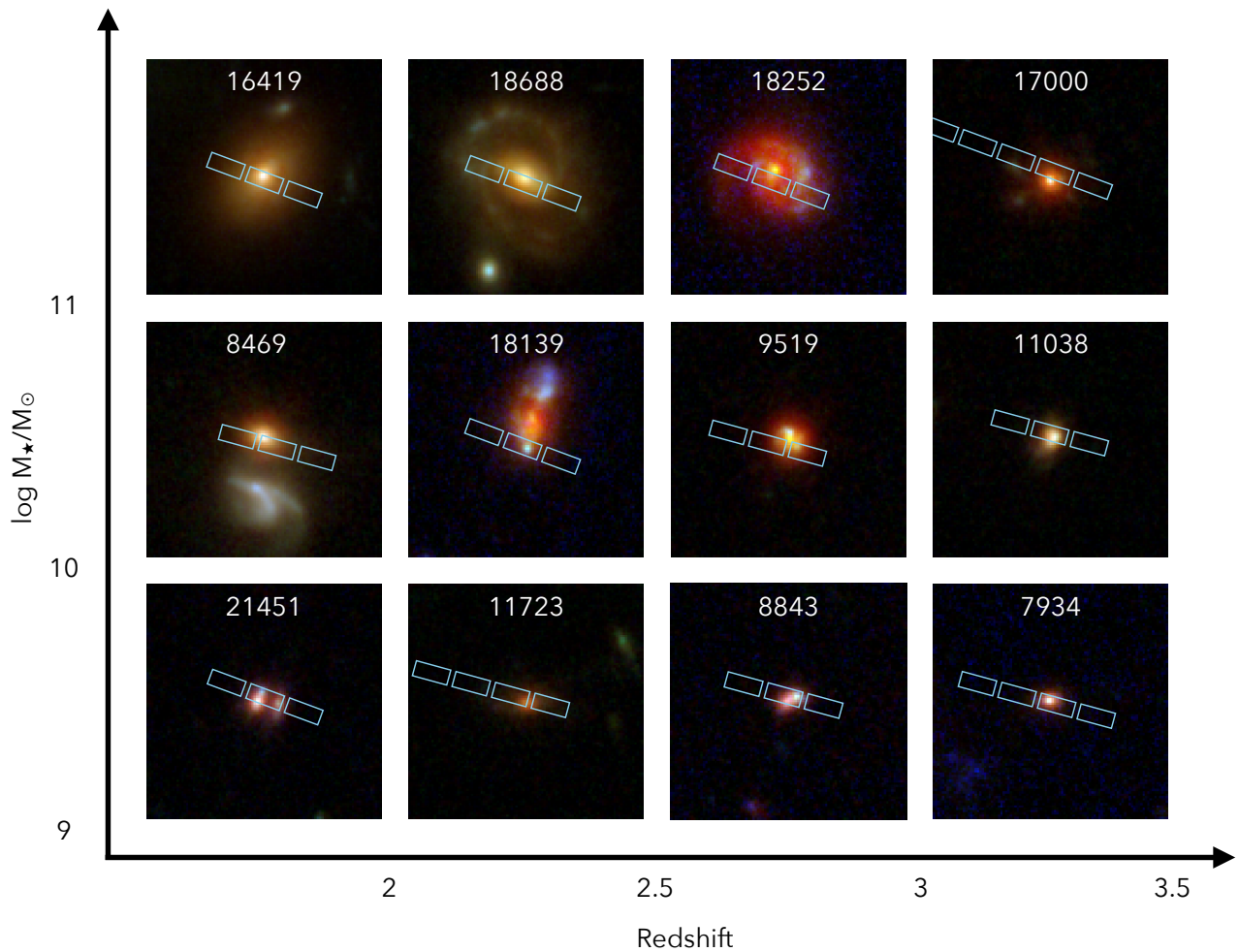


Fig. 11: A sample of Blue Jay spectroscopic targets spanning a range of redshifts and stellar masses. Cutouts are $3''$ on the side and are produced with the NIRCam F115W, F200W, F444W images; North is up. The footprint of the NIRSpec microshutters is shown in each cutout. The sum of the A and B nod positions is shown, so that 2-shutter slitlets span three shutter positions on the sky.

4.1. Photometric Data

All Blue Jay targets happen to be within the field observed by the PRIMER survey, a Cycle-1 program (GO 1837; PI: J. Dunlop) that obtained multi-band NIRCam observations in a subset of the COSMOS and UDS fields. PRIMER imaging includes seven broad-band filters (F090W, F115W, F150W, F200W, F277W, F356W, F444W) and one medium-band filter (F410M). These observations were taken after the Blue Jay survey was executed, so they were not used for the target selection. We reduce the public imaging data and tie the astrometry to the Gaia coordinates of reference stars.

We also adopt multi-band HST imaging taken with ACS (F606W and F814W) and WFC3 (F125W, F140W, F160W) in the COSMOS field as part of the CANDELS survey (Grogin et al. 2011; Koekemoer et al. 2011). We download the v7.0 mosaics of the HST imaging data for the PRIMER field from the Dawn JWST Archive². These mosaics are aligned with the DASH F160W mosaic and so we apply the same astrometric correction discussed in Section 2.2.

The scientific analysis of the Blue Jay sample is thus based on HST and JWST photometry in 13 filters covering from 6000 \AA to $4.4 \mu\text{m}$, corresponding to a complete coverage of the rest-frame optical wavelength range for galaxies at Cosmic Noon, including parts of the rest-frame UV and near-infrared range. This highly homogeneous, space-based data set is crucial for accurately measuring the photometry in the small box aperture, as described below. Additional imaging in about 40 bands is available for the COSMOS field from several ground-based observations. We used these observations for characterizing the parent sample during the preparation of the Blue Jay survey (see Section 2.3), however we do not employ ground-based data for the scientific analysis because of its poor spatial resolution.

4.2. Source Photometry

For each target, we use the NIRCam cutout in the F444W filter to calculate a segmentation map, from which we derive an elliptical aperture encompassing most of the emission belonging to the source. The segmentation map parameters are manually adjusted for complicated cases, e.g. when the galaxy is clumpy or is interacting with a companion. Next, we PSF-match all the JWST

² <https://dawn-cph.github.io/dja/>

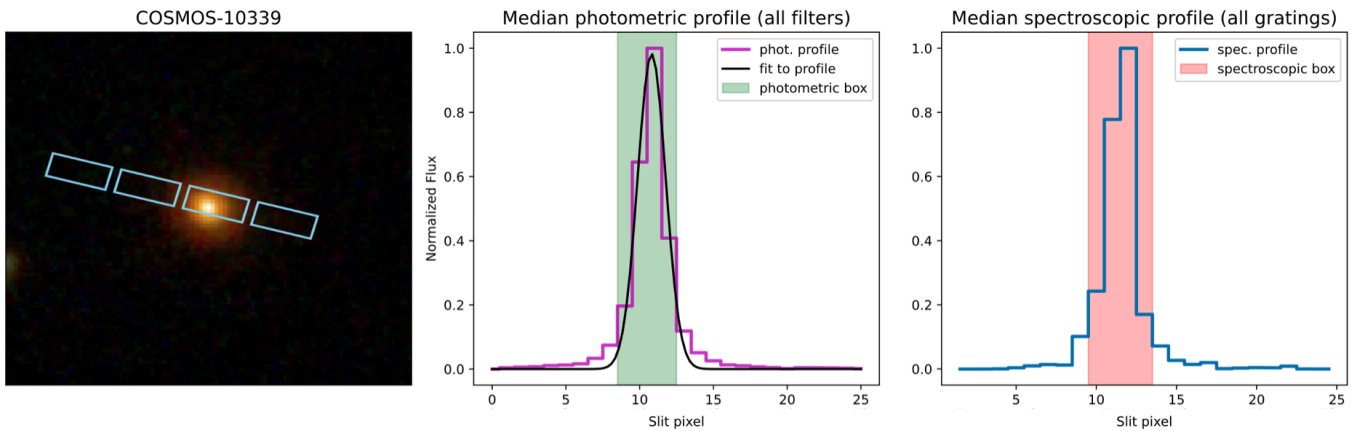


Fig. 12: Definition of the spectroscopic box for an example galaxy. Left: JWST/NIRCam cutout with the footprint of the NIRSpec slitlet. Center: photometric profile along the slitlet (purple line), obtained by calculating the median of all NIRCam filters resampled on the NIRSpec grid of 0''.1-pixels. The black line is the best-fit Gaussian profile, and the box photometry is extracted from the green region. Right: Spectroscopic profile along the slitlet (median of all three NIRSpec gratings), with the spectroscopic box shown in pink. There is a small offset between the photometric and spectroscopic box to account for the effect of bar shadows and misalignments.

and HST images to the reddest filter available on the same telescope, i.e. F444W on JWST and F160W on HST, which have nearly identical spatial resolution (FWHM of 0.14 arcsec). We then measure the photometry in the elliptical aperture (derived from F444W) for each PSF-matched image, and apply a theoretical aperture correction under the assumption of a point source.

The uncertainty on the source photometry is calculated from the flux error in each pixel for JWST/NIRCam data; while for HST bands we adopt the procedure developed by Skelton et al. (2014), which is based on the photometry measured for empty apertures and thus accounts for correlated errors. Finally, for each HST and JWST band we assess the possible presence of non-zero background due to, for example, imperfect data reduction. We estimate the background flux by measuring the median flux in all pixels that are near the source, after aggressively masking all detected objects. We find that the background is systematically consistent with zero, and we do not subtract it from the measured photometry; however we include the uncertainty on the determination of the background flux in the final photometric uncertainty of each source.

4.3. “Box” Photometry

For each source, in addition to the elliptical aperture we also define a smaller “box” aperture that is used for extracting both photometry and spectroscopy. We define the box in the following way: we take the footprint of the NIRSpec slitlet and treat it as if it was a single, solid slit (i.e. we neglect the shutter bars), then we measure the flux profile along the slit in each JWST/NIRCam band. We resample the flux profile on a grid matching the NIRSpec spatial pixels, which are 0''.10 on the side, and then median-stack the normalized profiles of all bands together; an example is shown in Figure 12. We fit the profile with a Gaussian profile and take the $\pm 2\sigma$ limits, rounded to the closest pixels, as the box limits. This choice is made in order to optimize the SNR of the 1D spectrum, since a longer box would include more light but also more readout noise. We measure the photometry and its uncertainty in the box aperture, for each of the HST and JWST filters that are available, using the PSF-matched cutouts.

Photometric measurements made through such a small aperture are extremely sensitive to the exact placement of the box on the cutout. We thus estimate the relative uncertainty on the box photometry due to a possible offset between the nominal and actual position of the NIRSpec slitlet on the galaxy image. There are two physical reasons for this offset:

1. The nominal position is based on the reference DASH mosaic described in Section 2.2, which has an uncertainty of 12 mas on the absolute astrometry as measured from the position of Gaia stars. This means that each cutout used for the photometry measurement cannot be aligned to the box aperture with a precision higher than this.
2. The NIRSpec “MSATA” acquisition procedure can position the slitlets with a limited accuracy, which depends on the astrometric precision of the reference mosaic used to prepare the observations³. Given the astrometric precision of our parent catalog, the NIRSpec pointing should have an uncertainty of 20 mas.

As a result, the uncertainty on the placement of the NIRSpec shutter footprint on any given mosaic of HST or JWST imaging is 23 mas on each coordinate. This is almost ten times smaller than the shutter width, which is 200 mas. For a uniformly illuminated slit this uncertainty on the position does not introduce any additional uncertainty on the flux measured through the slit. However, for a point source placed near the edge of the shutter the uncertainty can be non-negligible. We estimate an approximate value for this uncertainty by assuming that the PSF is a uniformly illuminated disk with a 140 mas diameter, which is the FWHM of the PSF-matched imaging (see Section 4.2). If the PSF is placed near the edge of the shutter, and the edge position is changed by 23 mas, then the area of the PSF falling in the shutter changes by at most $23/140 \sim 16\%$, causing a similar change in the measured flux. Considering that our typical target is substantially more extended than the size of the PSF, we adopt this

³ <https://jwst-docs.stsci.edu/jwst-near-infrared-spectrograph/nirspec-operations/nirspec-target-acquisition/nirspec-msa-target-acquisition>

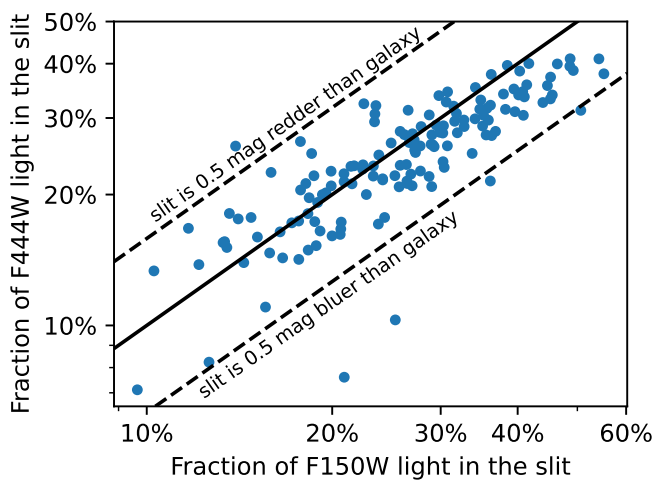


Fig. 13: Slit loss in F444W vs. slit loss in F150W for the Blue Jay sample. Slit loss is defined here as the flux measured in the spectroscopic box from which the NIRSpec 1D spectrum is extracted, divided by the flux measured for the entire source. The solid line is the 1:1 relation, where the colors of the spectroscopic aperture are the same as the galaxy colors. Dashed lines indicate where the colors measured in the spectroscopic aperture deviate by 0.5 mag compared to the colors measured for the entire galaxy.

as a conservative estimate of the systematic uncertainty in the slit photometry, to be added in quadrature to the flux uncertainty.

4.4. Extraction of 1-D Spectra

We aim to extract the NIRSpec 1D spectrum from the same box aperture used to extract the photometry. The first step is to obtain the median light profile along the slitlet, by collapsing the 2D spectrum on the spatial direction for all three gratings. When we compare this *spectroscopic* profile with the *photometric* profile we often find peaks at slightly different positions along the slitlet (see, for example, Figure 12). This is due to different reasons, such as inconsistent definitions of the zero-th pixel in the NIRSpec vs NIRCam data, and the presence of bar shadows in the 2D spectrum. We measure a systematic offset in the profile peak of 0.7 pixels, which we apply to every spectroscopic profile. We then allow for a further shift of the box by up to ± 2 pixels, by calculating the box position that maximizes the spectroscopic SNR. We repeat this procedure separately for each of the three gratings, and define our final spectroscopic box as the one that maximizes the SNR for the majority of the gratings. This procedure ensures that both the photometry and the spectroscopy come from an equal-size box along the slitlet that encompasses the peak of the light emitted by the source.

Finally, 1D spectra are extracted using a simple boxcar extraction from the selected region along the slit. We decide not to use the optimal extraction algorithm (Horne 1986) because it makes it difficult to build a dataset of matching spectroscopic and photometric data extracted from the same region. The optimal extraction guarantees a higher SNR, but we verified that the increase in SNR compared to our boxcar extractions is marginal for the majority of the sample.

4.5. Slit losses

Using the two sets of measurements — the source photometry and the box photometry — we are now able to assess the fraction of light emitted from each source that is captured by the NIRSpec spectrum. We define the “slit loss” in a given band as the ratio between the flux measured in the box aperture and the total source flux measured in the elliptical aperture. We note that this measurement does not account for the light lost to the shutter bars; also, slit loss is somewhat a misnomer because we are not considering the full extent of the slit, but only the small box aperture which is used to extract the 1D spectrum.

Figure 13 shows the distribution of slit losses for the Blue Jay sample, calculated in the F444W and F150W NIRCam bands. Generally, less than 50% of the light falls in the spectroscopic aperture, and this fraction can be as low as 7% for the most extreme cases such as 18139 (one of the examples shown in Figure 11), where the slitlet goes through a small, HST-detected clump that belongs to a much larger, HST-dark galaxy.

By comparing the slit loss in different bands we can also assess whether the region targeted by NIRSpec is representative of the whole galaxy. The bulk of the sources in Figure 13 lie near the 1:1 line, where the slit loss is the same in blue and red filters; however the scatter is large and can reach 0.5 magnitudes of difference in either direction. This means that the spectroscopic measurements of star formation rates, stellar ages, etc. are not those of the entire galaxy, but only of the region targeted by NIRSpec which is often, but not always, the central one. Moreover, this introduces a systematic effect when fitting simultaneously the spectroscopy derived from the box aperture with the photometry derived from the large elliptical aperture: the two data sets are inconsistent as they belong to regions with different physical properties. This problem has generally been of limited impact for ground-based spectroscopic observations given the combination of large PSF and large slit width. However, the small size of the NIRSpec shutters compared to the typical size of galaxies at Cosmic Noon makes it particularly important to match the spectroscopic and photometric apertures. By employing the box photometry we are now able to model both spectroscopic and photometric data in a self-consistent way; this analysis is presented in Bugiani et al. (2025, in prep.).

4.6. Data Release

We release the HST and JWST photometry for each Blue Jay target, measured from both the elliptical and the box apertures, in the public repository <https://doi.org/10.5281/zenodo.17333505>. We also release the spectroscopic data set, including the 2D spectra obtained both with the master background subtraction and with the $A - B$ subtraction; the 1D spectra extracted from the box aperture; the NIRCam cutouts showing the shutter footprint; catalogs for the target and parent samples including the spectroscopic weights; and the custom MSA metafiles used for the data reduction, in the public repository <https://doi.org/10.5281/zenodo.17343094>. The photometric and spectroscopic data set released with the present work have been labeled v2 to distinguish them from earlier versions adopted (and publicly released) by previous works (e.g., Belli et al. 2024; Park et al. 2024). The v2 data reduction represents a substantial improvement over previous versions, which included fewer targets due to failures in the data reduction and did not employ the matched-aperture extraction of spectroscopy and photometry.

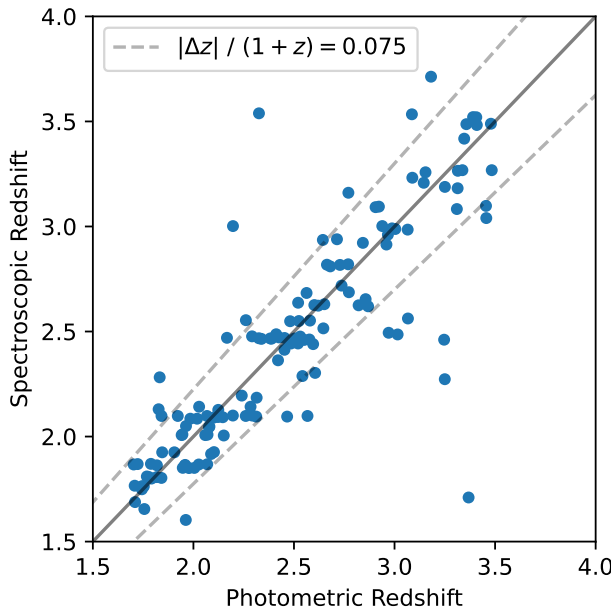


Fig. 14: Comparison of spectroscopic and photometric redshifts. The black solid line is the 1:1 relation, while the dashed lines mark the standard deviation of the discrepancy.

5. The Blue Jay Sample

The vast majority of the 153 spectra contain a large number of emission and/or absorption lines, making it possible to measure redshifts without ambiguity. The four high-redshift filler targets are all confirmed as being at $z \sim 6 - 7$ via the detection of several emission lines; their spectra are shown in Appendix B. We remove these targets from the Blue Jay sample due to their different selection method. The Cosmic Noon sample thus consists of 149 galaxies, which we list in Table 4.

5.1. Spectroscopic Redshifts

We secure a spectroscopic redshift for 138 out of 149 galaxies, corresponding to a success rate of 93%. For the 11 failures we are unable to identify emission or absorption lines in the NIRSpec data, although a faint continuum is usually visible. Some of these spectra are affected by contamination due to stuck open shutters, which effectively reduces the wavelength range in which spectral features can be identified. In other cases, adding the NIRCam photometry (which was not available when the targets were selected) to the SED fit drastically changes the photometric redshift, revealing that four targets are likely at very low redshift, $z \sim 0.3$. In the end, only a handful of galaxies are probably in the correct redshift range and have emission lines that are simply too faint to be detected by NIRSpec.

Since the sample selection was based on the photometric redshifts, it is important to verify whether these redshifts are approximately correct for the majority of the sample. Figure 14 shows that in most cases the photometric redshifts are in excellent agreement with the spectroscopic redshifts. The standard deviation of the discrepancy is $(z_{\text{phot}} - z_{\text{spec}})/(1 + z_{\text{spec}}) = 0.075$, and only four galaxies are outliers, i.e. are discrepant beyond 3σ . Incidentally, the `Prospector` emulator performs substantially better than the photometric redshifts from the 3D-HST catalog, which have a standard deviation twice as large. The 3D-HST

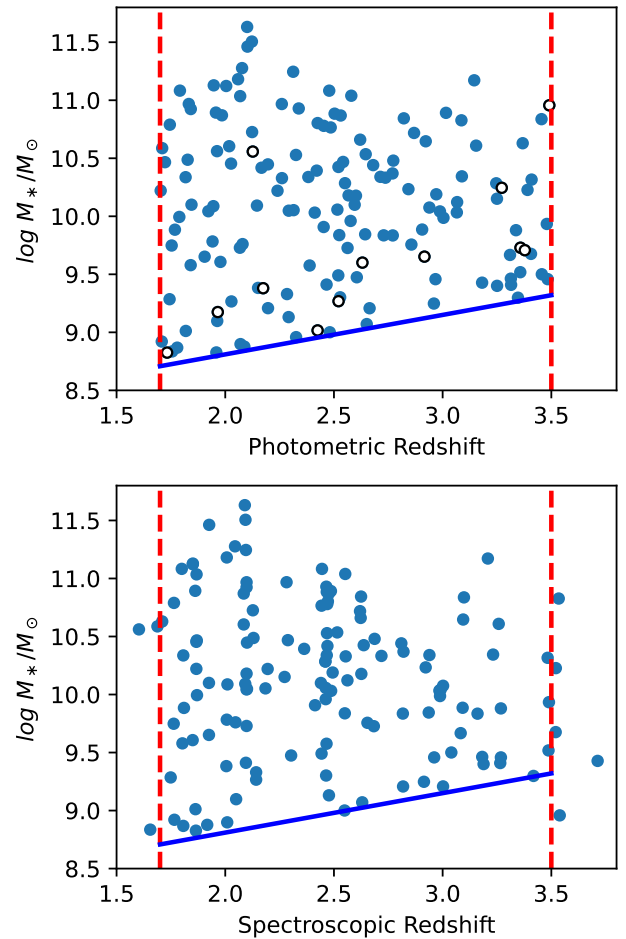


Fig. 15: Stellar mass vs. redshift for the Blue Jay sample, using photometric redshifts (top panel) and spectroscopic redshifts (bottom panel). Empty circles mark galaxies without spectroscopic redshift. Lines showing the limits in mass and redshift for the sample selection are the same as those in Figure 3. The overdensities at $z \sim 2.1$ and $z \sim 2.45$ are visible in the spectroscopic redshift distribution.

catalog includes four catastrophic outliers with $|\Delta z| \gtrsim 2$, which is likely similar to the number of catastrophic outliers for the `Prospector` emulator, if one includes the $z \sim 0.3$ galaxies for which we could not secure a spectroscopic redshift.

5.2. A Representative Sample

The top panel of Figure 15 shows the Blue Jay sample on the stellar mass vs. redshift plane used for the selection, and confirms that our spectroscopic observations probe this parameter space in a roughly uniform manner. This was achieved by adopting appropriate spectroscopic weights during the NIRSpec MSA planning, otherwise the number of low-mass and low-redshift galaxies would have been overwhelmingly larger, following the distribution of the parent sample shown in Figure 3.

The 11 galaxies with no spectroscopic redshift measurement, shown as empty circles in the figure, tend to be at low masses, near the mass selection limit. Their faintness helps explain why these galaxies have undetected emission lines in the NIRSpec

Table 4: The Blue Jay Sample

(1) ID	(2) R.A.	(3) Dec.	(4) F160W	(5) Weight	(6) $\log M_*/M_\odot$	(7) z_{phot}	(8) z_{spec}
7102	150.089834	2.250410	25.2	5	9.4	3.31	3.265
7136	150.106314	2.251556	23.2	19	11.1	2.00	1.851
7185	150.105835	2.251845	24.4	1	9.6	1.98	1.850
7549	150.120110	2.255571	24.3	22	10.7	2.62	2.623
7730	150.124647	2.257914	25.0	8	9.5	3.48	3.268
...							

Notes. The full table with 149 rows is available online; the 4 high-redshift fillers are not included (see Appendix B). (1) ID from the 3D-HST catalog for the COSMOS field (v4.1.5, [Skelton et al. 2014](#)); (2) and (3) coordinates measured from a mosaic of HST F160W data astrometrically registered with Gaia stars (see Section 2.2); (4) AB magnitude in F160W, from the 3D-HST catalog; (5) spectroscopic weight used for planning the MSA configuration (see Section 2.4); (6) and (7) stellar mass and photometric redshift measured with a `Prospector` emulator (see Section 2.3); (8) spectroscopic redshift measured from Blue Jay spectroscopy.

data, and also why in some cases their pre-JWST photometric redshifts were wrong.

The bottom panel of Figure 15 shows the sample distribution on the same stellar mass vs. redshift plane, but using spectroscopic instead of photometric redshifts. A few targets are now slightly outside the $1.7 < z < 3.5$ range, but this clearly does not substantially impact the overall redshift distribution of the sample. The most striking difference between the top and bottom panels, however, is the emergence of vertical patterns in the galaxy distribution when using the spectroscopic redshifts. These are overdense regions containing an excess of galaxies at the same redshift. Two overdensities are particularly noticeable: one at $z \sim 2.1$ ([Spitler et al. 2012](#)), which was included in the North pointing by design in order to optimize the number of massive galaxies; and another at $z \sim 2.45$, corresponding to the large-scale “Hyperion” proto-cluster ([Cucciati et al. 2018](#)). While the presence of overdensities in Blue Jay makes it possible to study galaxy properties as a function of environment, it also represents a source of bias in the sample since galaxies living in dense environments are likely overrepresented. This bias must be taken into account when analyzing the number density of Blue Jay targets (see, e.g., [Park et al. 2024](#)). Nonetheless this bias does not dominate the statistics of the sample, since the sum of the two overdensities accounts for only 30% of the total number of galaxies in the Blue Jay sample, and 40% of the massive systems ($\log M_*/M_\odot > 10.5$). Ultimately, the number density of Blue Jay targets is not limited only by the selection bias due to the placement of the pointing, but also by the substantial cosmic variance that affects small fields.

Finally, we consider whether the selection of the parent sample based on the HST F160W filter, which is relatively blue, may introduce a bias against very red systems. The launch of JWST enabled the discovery of a non-negligible population of sources that are bright in JWST/NIRCam imaging at 3-5 μm , but were previously undetected in HST observations (e.g., [Nelson et al. 2023](#); [Rodighiero et al. 2023](#); [Pérez-González et al. 2023](#); [Barrufet et al. 2023](#)). These so-called “HST-dark galaxies” are a mixed population, typically at $z > 2$, which include dusty galaxies, often seen edge-on, massive quiescent systems, and emission-line dominated galaxies. To investigate whether we are missing a large fraction of red galaxies from the parent sample, we make use of JWST/NIRCam observations in the COSMOS field by the PRIMER survey, which were not available when the Blue Jay sample selection was performed. Adopting the ASTRODEEP catalog by [Merlin et al. \(2024\)](#), which includes all sources detected in F356W + F444W and is therefore not biased

towards blue objects, we select all galaxies with photometric redshift in the range $1.7 < z < 3.5$ and plot their F160W–F444W color as a function of their F160W magnitude in Figure 16. Some of the sources have colors that are much redder compared to those of the main population. There is a clear trend where the red sources (which we define here with an arbitrary and conservative threshold of $\text{F160W} - \text{F444W} > 0.8$) represent a larger fraction of the population at the bright end, and nearly disappear at the low end. This is consistent with the physical nature of most of the red sources, which are either massive and quiescent or massive and dust-obscured galaxies. We can draw two important conclusions from Figure 16:

1. About 11% of the galaxies in the parent sample (i.e., with $\text{F160W} < H_{50}$) are red. These galaxies are, however, sufficiently bright to be detected by HST, and do not introduce a bias or incompleteness in our sample.
2. On the other hand, red sources that are fainter than H_{50} can potentially bias our sample, because they may be more massive than one would infer having access only to the HST data, and therefore might be above our mass limit $M_{\min} \sim 10^9 M_\odot$ (see Section 2.4), and yet not be part of the sample because of their faintness in HST imaging. However, at the faint end the fraction of red sources is low, only 3% for galaxies with $H_{50} < \text{F160W} < 28$, indicating that the vast majority of low-mass galaxies have blue colors.

We conclude that the population of HST-dark galaxies does not represent a substantial source of bias for the Blue Jay sample, because at these redshifts deep HST observations are able to capture the bulk of the galaxy population irrespective of their color. This bias is likely much more prominent at higher redshifts.

Finally, we note that the Blue Jay sample naturally includes interesting objects such as AGNs and mergers, since no filtering was applied to the parent sample. Three galaxies in the sample are detected in the X-rays (ID 12020, 11337, 19572), two are broad-line AGNs (12020, 18977), and several sources are involved in minor or major mergers. For a detailed study of the quiescent galaxy 12020 hosting a broad-line AGN detected in the X-rays, see [Ito et al. \(2025\)](#).

5.3. Overview of the Spectroscopic Data

The Blue Jay survey has obtained deep rest-optical spectroscopy for a representative sample of galaxies at Cosmic Noon. The key strengths of this program are 1) the wavelength coverage and

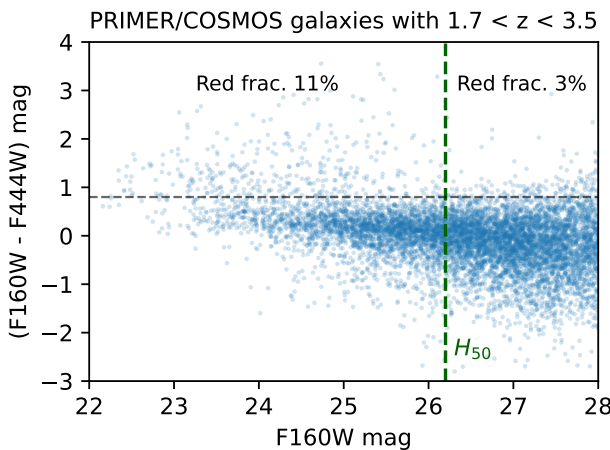


Fig. 16: Color-magnitude distribution of galaxies in the PRIMER/COSMOS catalog with $1.7 < z < 3.5$ from the ASTRODEEP catalog (Merlin et al. 2024). The green dashed line marks the completeness limit H_{50} for the HST catalog. The fraction of red galaxies is reported for the two subsamples of sources that are brighter and fainter than H_{50} . Red galaxies are defined as having $F160W - F444W > 0.8$, an empirical threshold that is shown as a horizontal dashed line.

depth of the spectroscopic observations, which enable the detection of a large number of spectral features in both absorption and emission; and 2) the careful selection of the targets, which allows one to study several types of galaxies free from strong selection biases.

We show two examples of Blue Jay spectra in Figure 17, one for a massive quiescent galaxy (in red) and one for a low-mass star-forming galaxy (in blue). The top panel shows the full wavelength range, obtained by combining the three medium-resolution gratings. The bluer grating, G140M, has a much deeper exposure and enables the study of numerous absorption lines for massive galaxies. These mostly originate from either hydrogen (Balmer series) or metals (Ca, Mg, Fe, and others) in the stellar photospheres, and can be used to measure the distribution of stellar ages and metal abundances. Moreover, the Na I D and Ca II H,K absorption lines are resonant (i.e., are transitions involving the ground level), and can therefore originate in cold gas in addition to the stellar photospheres. For this reason these lines can be used to probe cold neutral gas in or around galaxies.

The typical spectrum of star-forming galaxies, on the other hand, contains dozens of emission lines that can be used to study the physical properties of the interstellar medium. In the example spectrum shown in Figure 17 we detect many emission lines, from $[\text{O II}] \lambda 3727$ in the rest-frame UV to $\text{Pa} \beta$ in the rest-frame near-infrared, including the full rest-frame optical spectrum. The $\text{Pa} \beta$ line is outside the NIRSpec range for galaxies at the high-redshift end of the Blue Jay sample, but coverage up to $\text{Pa} \gamma$ is observed for every target in the $1.7 < z < 3.5$ range. Hydrogen lines in the Paschen and Balmer series can be used to derive the extinction curve and the star formation rate; while sets of lines corresponding to different ionization stages of the same element, such as $[\text{O II}]$ and $[\text{O III}]$ or $[\text{S II}]$ and $[\text{S III}]$, offer a direct probe of the ionization state of the gas. By combining metal and hydrogen lines it is also possible to measure metal abundances and detect the presence of shocks and/or photoionization by AGN.

6. Summary and Discussion

We presented the Blue Jay survey, a Cycle-1 JWST program that obtained deep NIRSpec spectroscopy for 153 sources in the COSMOS field, with the goal of studying the physical properties of galaxies at Cosmic Noon. Here we briefly summarize the most important aspects of this survey:

1. The sample was carefully selected in order to obtain a roughly uniform coverage of the mass-redshift plane within the range $1.7 < z < 3.5$ and $M_* > M_{\min}(z)$, where the stellar mass limit M_{\min} varies between $10^{8.7} M_{\odot}$ and $10^{9.3} M_{\odot}$ and ensures that we are complete to all types of galaxies at a given mass. The Blue Jay sample is representative of the Cosmic Noon population, without strong biases in any physical properties, and includes both star-forming and quiescent galaxies. The sample also spans a range of environments, with about 30% of the targets belonging to two known over-densities at $z = 2.1$ and $z = 2.45$.
2. We employ a non-standard observing strategy with the NIRSpec MSA, where each target is placed on a 2-shutter slitlet, and additional empty shutters are opened until all the space available on the detector is filled. We observe with an $A - B$ nodding pattern which is however used as a dither in order to avoid self-subtraction of large targets, while background subtraction is performed via a master background spectrum, constructed from the empty shutters. We validate the master background spectrum via comparison to the JBT model and to the small-scale features of the zodiacal light.
3. In order to perform a self-consistent analysis of the spectroscopic data together with HST and JWST broadband photometry, we extract the photometry from the same box aperture used to extract the 1D spectrum from the NIRSpec observations. We publicly release the matched spectro-photometric data set, together with photometry measured in a standard elliptical aperture.
4. Each target is observed with the G140M, G235M, and G395M gratings for 13 hours, 3.2 hours, and 1.6 hours respectively. The observations cover the full NIRSpec wavelength range, 1 to $5 \mu\text{m}$, corresponding to the entire rest-frame optical wavelength range. The $R \sim 1000$ resolution allows us to detect a wealth of emission lines, including the full range between $[\text{O II}] \lambda 3727$ and $\text{Pa} \gamma$ for every observed galaxy. Lines outside this range are observed in many galaxies, according to their redshift. The deeper observations in G140M enable the detection of Balmer and metal absorption lines in massive galaxies. We unambiguously identify the spectroscopic redshift for 93% of the sample.

Several scientific results have already been obtained with the Blue Jay spectra, with an emphasis on constraining the physical processes responsible for galaxy quenching. Park et al. (2024) measured the star formation histories of 14 massive quiescent galaxies, finding that most systems experienced rapid quenching, either with or without a preceding starburst. By analyzing the emission lines in the same sample, Bugiani et al. (2025) detected the widespread presence of low-luminosity AGN activity. Access to the Na I D absorption line, which is extremely difficult to detect in ground-based spectroscopy, has allowed Davies et al. (2024) to discover powerful neutral outflows, which appear to be very common among massive galaxies at Cosmic Noon, irrespective of their star formation rate. Liboni et al. (2025) confirmed this result by using the alternative Ca II H, K doublet as a neutral gas diagnostic. When considering these results, a consistent picture is emerging: massive galaxies likely experience a

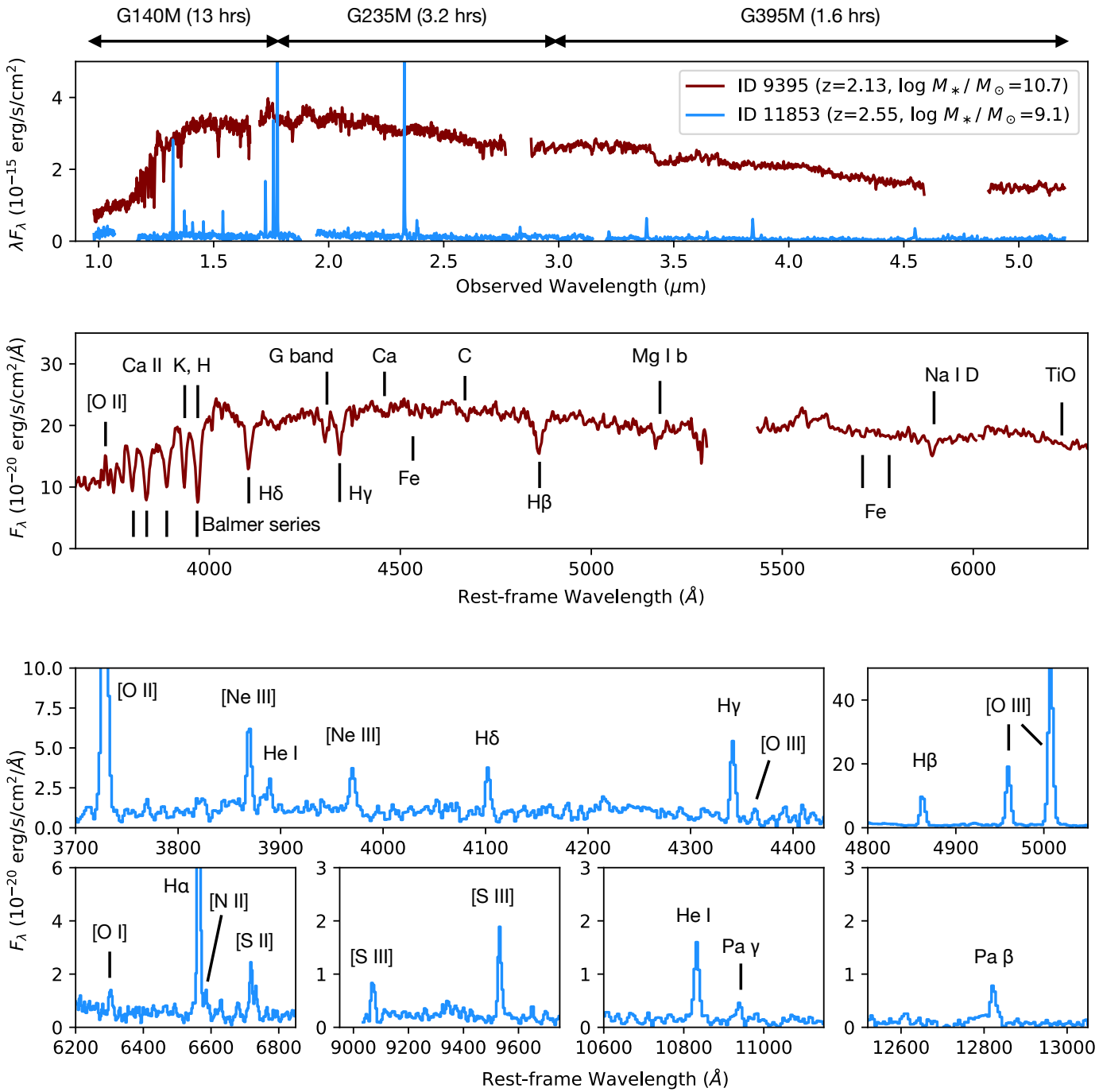


Fig. 17: Example spectra for a massive quiescent galaxy (ID 9395, in red) and a low-mass star-forming galaxy (ID 11853, in blue). *Top panel:* Full spectrum (plotted as λF_λ) for both galaxies covering the full range 1–5 μm . The wavelength range and exposure time for each of the three medium-resolution gratings are shown above the panel. *Middle panel:* Zoom-in of the quiescent galaxy spectrum in the rest-frame optical region observed with the G140M grating, showing numerous absorption lines. *Bottom panels:* Zoom-ins on several emission lines detected in the star-forming galaxy, ranging from the rest-frame UV to the rest-frame near-infrared.

rapid shutdown of star formation following rapid evacuation of their cold gas reservoir via powerful AGN-driven outflows. In at least one case, the massive galaxy 11142 at $z = 2.45$ analyzed by Belli et al. (2024), the Blue Jay spectrum clearly reveals all the elements of this physical picture: a rapid and recent quenching, a low-luminosity AGN, a weak ionized outflow probed by emission lines, and a powerful neutral outflow probed by resonant absorption lines. The measurement of these physical properties in the same galaxy, which happens to be observed immediately after a rapid shutdown of its star formation, represents a rare

case in which the link between AGN feedback, outflows, and quenching can be directly established. This link, and the importance of the neutral phase in the overall gas budget, has been independently confirmed by other JWST observations of recently-quenched galaxies at Cosmic Noon and even higher redshift (e.g. D’Eugenio et al. 2024; Wu 2025; Valentino et al. 2025; Sun et al. 2025).

In addition to the study of stellar populations, ionized gas, and neutral gas, the Blue Jay spectra constrain the properties of dust as well, as shown by Maheson et al. (2025) who compare

the dust attenuation measured from spectral fitting to that derived from the Balmer emission line ratios. Further analysis of the Blue Jay sample is ongoing, including studies of the stellar abundances and kinematics, morphology, environment, dust attenuation curve, and properties of the interstellar medium.

The Blue Jay sample is also ideal for building follow-up campaigns with other facilities, to expand the set of physical properties that can be measured for the same galaxies. Scheduled ALMA observations will soon enable the detection of molecular gas reservoirs in some of the Blue Jay massive galaxies; while ground-based optical spectroscopy is being obtained to extend the study of absorption lines of both interstellar and stellar origin into the rest-frame UV. Finally, nearly the full sample has been re-observed in Cycle 3 with JWST/NIRSpec using the high-resolution G235H grating, with the goal of spectrally resolving the Na I D and H α lines and obtaining a detailed measurement of the gas kinematics in the neutral and ionized phases.

Acknowledgements. SB acknowledges helpful discussions about the NIRSpec data reduction with Ryan Trainor, Gwen Rudie, and the CECILIA team. This research was supported by the International Space Science Institute (ISSI) in Bern, through ISSI International Team project 24-602 "Multiphase Outflows in Galaxies at Cosmic Noon". The Blue Jay Survey is funded in part by STScI Grant JWST-GO-01810. SB, LB, AHK and CL are supported by ERC grant 101076080 "Red Cardinal". MP acknowledges support from the Kavli Institute for Cosmology, Cambridge and the Kavli Foundation. RLD is supported by the Australian Research Council through the Discovery Early Career Researcher Award (DECRA) Fellowship DE240100136 funded by the Australian Government. RW acknowledges funding of a Leibniz Junior Research Group (project number J131/2022). This work is based on observations made with the NASA/ESA/CSA James Webb Space Telescope. The data were obtained from the Mikulski Archive for Space Telescopes at the Space Telescope Science Institute, which is operated by the Association of Universities for Research in Astronomy, Inc., under NASA contract NAS 5-03127 for JWST. These observations are associated with program GO 1810 and GO 1837. This work also makes use of observations taken by the 3D-HST Treasury Program (GO 12177 and 12328) with the NASA/ESA HST, which is operated by the Association of Universities for Research in Astronomy, Inc., under NASA contract NAS 5-26555.

Kriek, M., Beverage, A. G., Price, S. H., et al. 2024, ApJ, 966, 36
 Kriek, M., Shapley, A. E., Reddy, N. A., et al. 2015, ApJS, 218, 15
 Kriek, M., van Dokkum, P. G., Labb  , I., et al. 2009, ApJ, 700, 221
 Kurucz, R. L. 1993, SYNTHE spectrum synthesis programs and line data
 Leja, J., Johnson, B. D., Conroy, C., et al. 2019, ApJ, 877, 140
 Leja, J., Johnson, B. D., Conroy, C., van Dokkum, P. G., & Byler, N. 2017, ApJ, 837, 170
 Liboni, C., Belli, S., Bugiani, L., et al. 2025, arXiv e-prints, arXiv:2506.05470
 Madau, P. & Dickinson, M. 2014, ARA&A, 52, 415
 Maheson, G., Tacchella, S., Belli, S., et al. 2025, arXiv e-prints, arXiv:2504.15346
 Maseda, M. V., Lewis, Z., Matthee, J., et al. 2023, ApJ, 956, 11
 Mathews, E. P., Leja, J., Speagle, J. S., et al. 2023, ApJ, 954, 132
 Mendel, J. T., Beifiori, A., Saglia, R. P., et al. 2020, ApJ, 899, 87
 Merlin, E., Santini, P., Paris, D., et al. 2024, A&A, 691, A240
 Momcheva, I. G., Brammer, G. B., van Dokkum, P. G., et al. 2016, ApJS, 225, 27
 Mowla, L. A., Cutler, S. E., Brammer, G. B., et al. 2022, ApJ, 933, 129
 Muzzin, A., Marchesini, D., Stefanon, M., et al. 2013, ApJ, 777, 18
 Nelson, E. J., Suess, K. A., Bezanson, R., et al. 2023, ApJ, 948, L18
 Onodera, M., Renzini, A., Carollo, M., et al. 2012, ApJ, 755, 26
 Park, M., Belli, S., Conroy, C., et al. 2024, ApJ, 976, 72
 P  rez-Gonz  lez, P. G., Barro, G., Annunziatella, M., et al. 2023, ApJ, 946, L16
 Pozzetti, L., Bolzonella, M., Zucca, E., et al. 2010, A&A, 523, A13
 Rigby, J. R., Lightsey, P. A., Garc  a Mar  n, M., et al. 2023, PASP, 135, 048002
 Rodighiero, G., Bisigello, L., Iani, E., et al. 2023, MNRAS, 518, L19
 Rogers, N. S. J., Strom, A. L., Rudie, G. C., et al. 2025, arXiv e-prints, arXiv:2509.18257
 Shapley, A. E., Sanders, R. L., Topping, M. W., et al. 2025, ApJ, 980, 242
 Skelton, R. E., Whitaker, K. E., Momcheva, I. G., et al. 2014, ApJS, 214, 24
 Slob, M., Kriek, M., Beverage, A. G., et al. 2024, ApJ, 973, 131
 Spitler, L. R., Labb  , I., Glazebrook, K., et al. 2012, ApJ, 748, L21
 Steidel, C. C., Rudie, G. C., Strom, A. L., et al. 2014, ApJ, 795, 165
 Steidel, C. C., Shapley, A. E., Pettini, M., et al. 2004, ApJ, 604, 534
 Stern, D. & Spinrad, H. 1999, PASP, 111, 1475
 Strom, A. L., Rudie, G. C., Trainor, R. F., et al. 2023, ApJ, 958, L11
 Sun, Y., Ji, Z., Rieke, G. H., et al. 2025, arXiv e-prints, arXiv:2504.14682
 Tal, T., Dekel, A., Oesch, P., et al. 2014, ApJ, 789, 164
 Valentino, F., Heintz, K. E., Brammer, G., et al. 2025, A&A, 699, A358
 van der Sande, J., Kriek, M., Franx, M., et al. 2013, ApJ, 771, 85
 van der Wel, A., Franx, M., van Dokkum, P. G., et al. 2014, ApJ, 788, 28
 Wang, B., Leja, J., Labb  , I., et al. 2024, ApJS, 270, 12
 Wisnioski, E., F  rster Schreiber, N. M., Wuyts, S., et al. 2015, ApJ, 799, 209
 Wu, P.-F. 2025, ApJ, 978, 131

References

Barrufet, L., Oesch, P. A., Weibel, A., et al. 2023, MNRAS, 522, 449
 Belli, S., Newman, A. B., & Ellis, R. S. 2014, ApJ, 783, 117
 Belli, S., Newman, A. B., & Ellis, R. S. 2017, ApJ, 834, 18
 Belli, S., Park, M., Davies, R. L., et al. 2024, Nature, 630, 54
 Bezanson, R., van Dokkum, P., van de Sande, J., Franx, M., & Kriek, M. 2013, ApJ, 764, L8
 Brammer, G. B., van Dokkum, P. G., & Coppi, P. 2008, ApJ, 686, 1503
 Brammer, G. B., van Dokkum, P. G., Franx, M., et al. 2012, ApJS, 200, 13
 Bugiani, L., Belli, S., Park, M., et al. 2025, ApJ, 981, 25
 Bushouse, H., Eisenhamer, J., Dencheva, N., et al. 2024, JWST Calibration Pipeline
 Carnall, A. C., McLure, R. J., Dunlop, J. S., et al. 2019, MNRAS, 490, 417
 Cataldi, E., Belfiore, F., Curti, M., et al. 2025, arXiv e-prints, arXiv:2504.03839
 Conroy, C. & Gunn, J. E. 2010, ApJ, 712, 833
 Conroy, C., Gunn, J. E., & White, M. 2009, ApJ, 699, 486
 Conroy, C., Johnson, B. D., van Dokkum, P., et al. 2024, ApJ, 968, 129
 Cucciati, O., Lemaux, B. C., Zamorani, G., et al. 2018, A&A, 619, A49
 Curti, M., Maiolino, R., Cirasuolo, M., et al. 2020, MNRAS, 492, 821
 Davies, R. L., Belli, S., Park, M., et al. 2024, MNRAS, 528, 4976
 de Graaff, A., Brammer, G., Weibel, A., et al. 2025, A&A, 697, A189
 Delvecchio, I., Gruppioni, C., Pozzi, F., et al. 2014, MNRAS, 439, 2736
 D'Eugenio, F., P  rez-Gonz  lez, P. G., Maiolino, R., et al. 2024, Nature Astronomy, 8, 1443
 F  rster Schreiber, N. M., Genzel, R., Bouch  , N., et al. 2009, ApJ, 706, 1364
 F  rster Schreiber, N. M. & Wuyts, S. 2020, ARA&A, 58, 661
 Gaia Collaboration, Vallenari, A., Brown, A. G. A., et al. 2023, A&A, 674, A1
 Grogin, N. A., Kocevski, D. D., Faber, S. M., et al. 2011, ApJS, 197, 35
 Horne, K. 1986, PASP, 98, 609
 Ilbert, O., McCracken, H. J., Le F  vre, O., et al. 2013, A&A, 556, A55
 Ito, K., Tanaka, T. S., Shimasaku, K., et al. 2025, MNRAS, 538, 1501
 Johnson, B. D., Leja, J., Conroy, C., & Speagle, J. S. 2021, The Astrophysical Journal Supplement Series, 254, 22
 Koekemoer, A. M., Faber, S. M., Ferguson, H. C., et al. 2011, ApJS, 197, 36

Appendix A: Stellar Mass Completeness of the Parent Sample

Since we select targets based on their stellar masses, we need to translate the completeness of the parent catalog from H -band magnitude to stellar mass. The mass completeness will depend on redshift and on the mass-to-light ratio distribution of the galaxies that are *not* observed. We derive this mass-to-light ratio distribution from a reference sample of galaxies selected in the following way: we first exclude objects fainter than H_{90} , since they are potentially affected by incompleteness, and then we take, at each redshift, the least massive half of the remaining galaxies. This reference sample, shown in red in the left panel of Figure A.1, is bright enough to be unbiased, but also low-mass enough to be representative of the galaxies that are missed by the parent catalog.

Following the method developed by [Pozzetti et al. \(2010\)](#), for each galaxy in the reference sample we calculate its limiting mass, defined as the stellar mass it would need to have to be observed exactly at H_{50} , assuming the same redshift and mass-to-light ratio. The limiting mass is given by $\log M_{\text{lim}} = \log M_* - 0.4 \cdot (H_{50} - H)$. The right panel of Figure A.1 shows the limiting masses for the reference sample: at each redshift they span a range of about one order of magnitude, reflecting the underlying range in mass-to-light ratios. We define the mass completeness level as the top 90th percentile of the M_{lim} distribution as a function of redshift (black line). Within the redshift limits of Blue Jay, the mass completeness is well represented by a linear fit: $\log M_{\text{min}}/M_\odot = 8.13 + 0.34z$ (blue line).

Since we used H_{50} to calculate M_{min} , the resulting target sample will be slightly biased near the mass completeness limit. A more rigorous completeness limit would need to be calculated using H_{90} , yielding $\log M_{\text{min}}^{90} = \log M_* - 0.4 \cdot (H_{90} - H) = \log M_{\text{min}} + 0.4 \cdot (H_{50} - H_{90}) = \log M_{\text{min}} + 0.36$. To assess the importance of incompleteness, we analyze the properties of galaxies with masses below M_{min}^{90} and above the completeness limit. We find that half of these galaxies are brighter than H_{90} , and the vast majority of them are much brighter than H_{50} . As a result, our parent catalog misses only 15% of the galaxies with $M_{\text{min}} < M_* < M_{\text{min}}^{90}$.

Appendix B: High-Redshift Filler Targets

Four filler targets out of 153 targets are selected with a dropout technique, and are therefore removed from the main Blue Jay sample. Multiple emission lines are detected for each of these four galaxies, yielding spectroscopic redshifts in the range $5.7 < z < 7$, in agreement with the photometric redshifts estimated through the dropout selection. Parts of the spectra of the four fillers are displayed in Figure B.1. The top panels show a dozen emission lines, from C III] 1909 to H α , detected for galaxy 11247 across the full wavelength range probed by the three NIRSpec gratings. The bottom panels show the H α emission for 7696 and 21026; and the H β and [O III] emission for 19945, for which H α falls outside the NIRSpec wavelength range due to the slightly higher redshift.

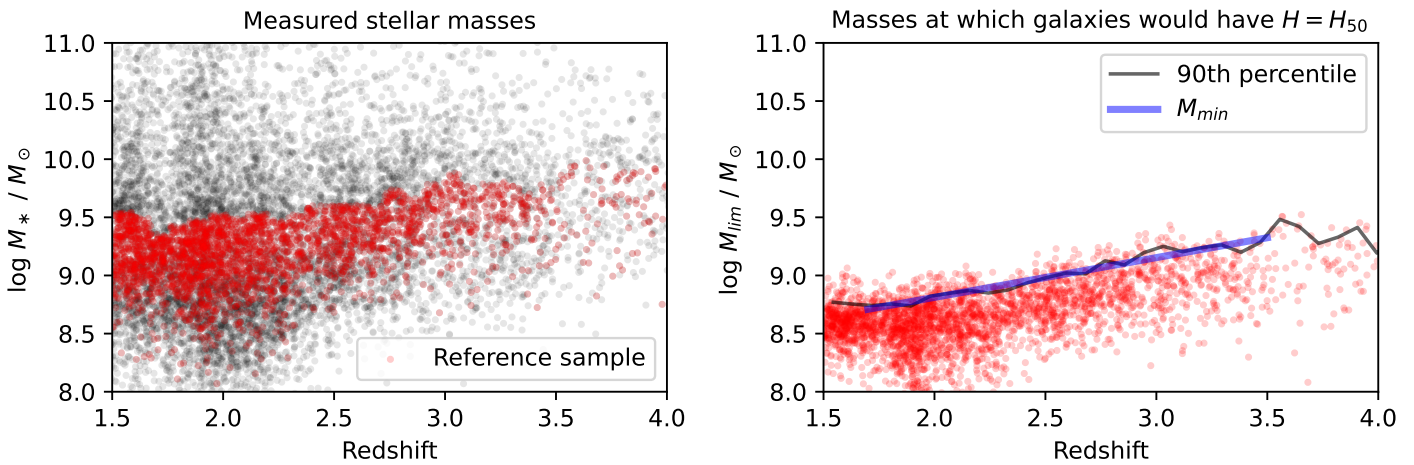


Fig. A.1: Assessing the mass completeness for the parent sample. *Left:* Stellar mass vs. redshift for the parent sample. The reference sample, shown in red, is defined as the least massive half of all galaxies that, at a given redshift, are brighter than H_{90} . *Right:* M_{lim} vs. redshift for the reference sample. For each galaxy we define M_{lim} as the mass it would need to have in order for its H band magnitude to equal H_{50} , assuming that redshift and mass-to-light ratio are unchanged. The blue line marks M_{min} , which is the top 90-th percentile of the M_{lim} distribution at each redshift.

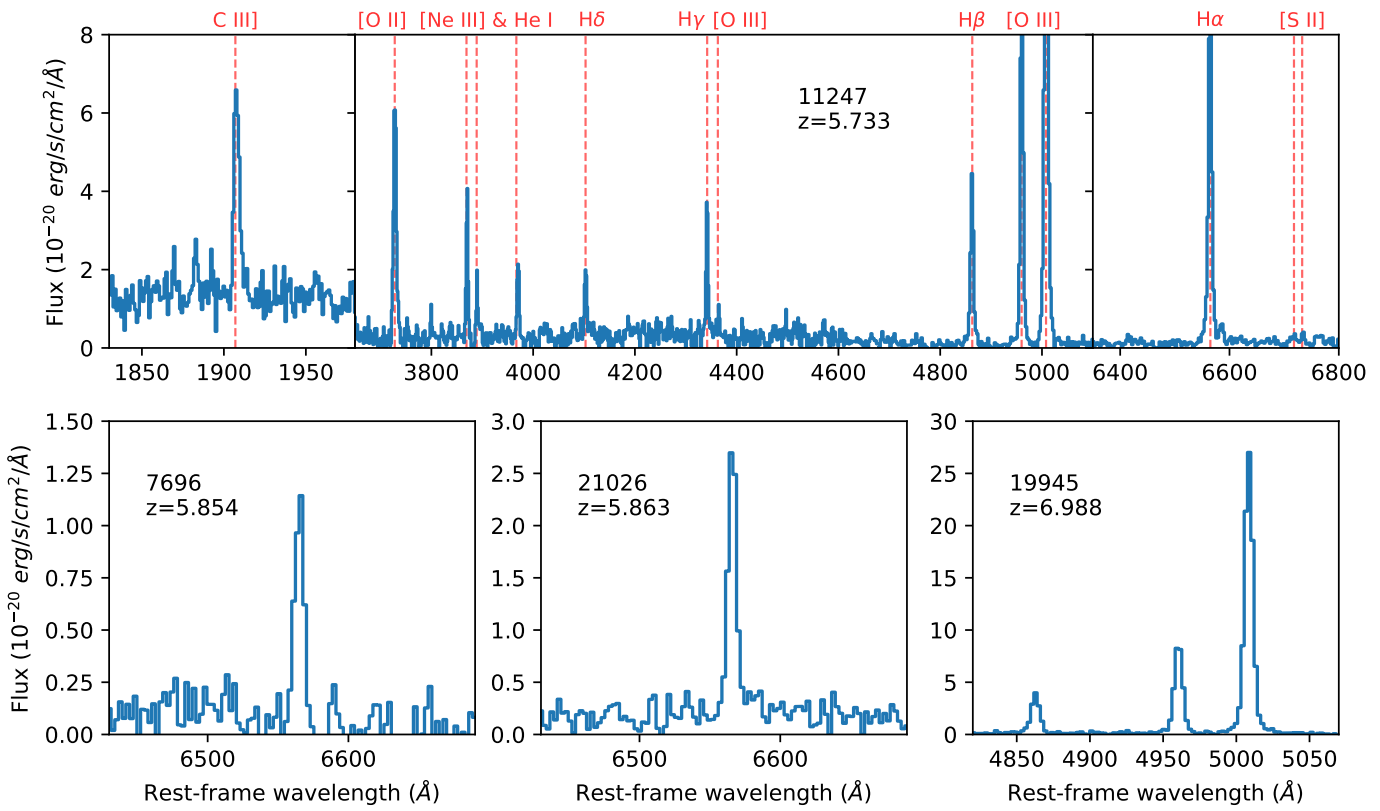


Fig. B.1: Spectra for the four filler targets at high redshift ($z \sim 6 - 7$). The top panels show the spectrum of 11247 with the position of strong emission lines marked, from the rest-UV to the rest-optical. The bottom panels show the H α emission line (or, in the case of 19945, H β and [O III]) for each of the other targets.